Comput. Methods Appl. Mech. Engrg. 266 (2013) 57–69

Contents lists available at SciVerse ScienceDirect

Comput. Methods Appl. Mech. Engrg.

journal homepage: www.elsevier.com/locate/cma

A finite-element/boundary-element method for large-displacement fluid–structure interaction with potential flow

T.M. van Opstal [a,*], E.H. van Brummelen [a,b]

[a] Mechanical Engineering, Eindhoven University of Technology, Postbox 513, 5600MB Eindhoven, The Netherlands
[b] Mathematics and Computer Science, Eindhoven University of Technology, Postbox 513, 5600MB Eindhoven, The Netherlands

ARTICLE INFO

Article history:
Received 13 October 2012
Received in revised form 12 July 2013
Accepted 15 July 2013
Available online 25 July 2013

Keywords:
Fluid–structure interaction
Inflatable structures
Boundary element method (BEM)
Strong coupling

ABSTRACT

This work concerns the interaction of light membrane structures enclosing incompressible fluids. Large displacements and collapsed boundaries (initially slender subdomains) are characteristic of this class of problems. A finite-element/boundary-element (FE/BE) coupled discretization is presented as an enabling technology, addressing these challenges by avoiding volumetric meshing as required by arbitrary Lagrangian Eulerian or immersed boundary type methods. The presented formulation includes a compatibility condition, to which a physical interpretation is given; and a regularizing bending stiffness, observed to be necessary from both the theoretical (well-posedness) and numerical (stability) point of view. A cheap contact load is designed to deal with possibly complex geometries, reusing already computed discrete boundary element kernels. Numerical experiments show the capabilities of the proposed scheme.

1. Introduction

Inflatable structures appear in a wide variety of engineering applications, e.g., evacuation slides in aircraft, air beams for temporary civil structures, stowable space structures, parachutes and air cushions. One of the most prominent examples of an inflatable structure is the airbag. Airbags form an indispensable component of passenger-safety systems in modern cars. Statistics of the US National Highway Traffic Safety Agency (NHTSA) corroborate that airbags yield a significant reduction in the fatality risk in frontal crashes, provided that the passenger is in position with respect to the airbag. On the other hand, US National Highway Traffic Safety Agency (NHTSA) investigations have shown that airbags can form an important safety *risk* in out-of-position situations. Airbags deploy at more than 300 km/h with an impact force exceeding 5 kN and, hence, an airbag can severely injure or kill a passenger if impact occurs before full deployment. Incentivized by the danger of airbags in out-of-position situations, the US National Highway Traffic Safety Agency (NHTSA) has issued new regulations that require car manufacturers to develop auxiliary restraint systems and new airbag systems to prevent such situations.

Numerical airbag-deployment simulations can provide valuable information in the assessment and control of out-of-position risks. Reliable numerical simulation of airbag-deployment dynamics is a complicated endeavor, however, on account of the inherent multi-scale character of the inflation process. The initial stowed or folded configuration of the airbag forms a complex labyrinth of small folds with a characteristic length scale that is orders of magnitude smaller than that of the bulbous final configuration. On the macroscale associated with the final configuration, the flow of the inflator gas exhibits highly complex behavior, on account of its multi-component composition, high temperature gradients, and a wide spectrum of flow velocities, extending over subsonic, transonic and supersonic regimes. On the microscale pertaining to the small folds, compressibility effects are negligible and the flow exhibits relatively simple behavior. The complexity of the airbag-deployment process is further compounded by self-contact of the airbag fabric, which is particularly manifest in the initial stages of the deployment process. Hence, airbag-deployment processes constitute fluid–structure interaction (FSI) problems with contact, in which the characteristic length scale of the geometry changes by many orders of magnitude, and each of the length scales must be adequately resolved in the numerical method to arrive at a reliable prediction of the dynamical behavior.

Many related and challenging fluid–structure interaction (FSI) computations have been performed with a wide array of methods, such as interface tracking [20,29,33,34] and interface capturing [6,17,25,42,39] techniques. Intrinsically, these methods, being based on discretizations of the volume occupied by the fluid, are not employed in the analysis of realistic stowed configurations on account of the geometrical complexity of the domain as well as the very large displacements. For that reason, in industrial applications the load on the airbag fabric is determined by overly

* Corresponding author. Tel.: +31 402472271.
E-mail address: t.m.v.opstal@tue.nl (T.M. van Opstal).

0045-7825/$ - see front matter © 2013 Elsevier B.V. All rights reserved.
http://dx.doi.org/10.1016/j.cma.2013.07.009

simplified fluid models, e.g., uniform-pressure models or empirical expressions. Such simplified models lack detailed information about the underlying physical processes, and generally cannot capture and predict the phenomena observed during experiments [24]. Recently, computational methods composed of particle-based approximation methods for the fluid, analogous to smoothed-particle hydrodynamics [27], have emerged [18]. The resolution provided by the moving particles in such approaches is uncontrollable, however, and on account of the large displacements that occur in airbag-deployment processes, the accuracy of particle-based methods is questionable.

The fundamental conundrum in airbag-deployment simulations, is that the scale disparity is so severe that the volumetric approximation methods that are suitable on the macroscale, cannot be employed on the microscale. The geometric complexity of the initial configuration precludes volumetric meshing with adequate resolution, even with adaptive interface-capturing or interface-tracking techniques [6,17]. However, conversely, the flow model that underlies volumetric approximation methods, viz., the Euler or Navier–Stokes equations, appears unnecessarily sophisticated for the flow in the small-scale features of the airbag. It is anticipated that the flow in small-scale features can be represented by a simplified model, without essentially degrading the accuracy of the prediction of the dynamics of the airbag on the large scales. Airbag-deployment simulation therefore necessitates an adaptive multiscale approach of type-A [12] in which the flow in the small-scale features of the airbag is resolved by a different model than the flow in the large-scale features.

The boundary-integral equation can be conceived of as a microscale model for the fluid flow in small-scale features of airbags or, more generally, inflatable structures. In the present work, a fluid–structure interaction (FSI) model for inflatable structures based on a boundary-integral formulation of the fluid is considered. The considerations are restricted to a 2D potential-flow model, but the investigation extends mutatis mutandis to for instance Stokes flow, which is treated in [37]. The connection to a macroscale model for the flow in the large-scale features and the corresponding model adaptivity is treated in [35]. The essential attribute of the boundary-integral formulation is that it provides an adequate model for the flow in the small-scale features of airbags, which does not require a volumetric mesh. In particular, the boundary-integral equation is set on the manifold of codimension one formed by the fluid–structure interface. The corresponding boundary element method (BEM) is therefore invulnerable to the extreme deformations that occur in airbag-deployment processes. An additional advantage of the boundary-integral formulation in the context of fluid–structure interaction (FSI) problems, is that it provides a very efficient model, as the domain of the flow model is restricted to the domain where the interaction with the structure actually occurs, viz., the fluid–structure interface.

The membrane in 2D is modeled as a linearly-elastic string [41,1], regularized by a small flexural rigidity. The membrane equation is approximated by means of a standard finite-element discretization based on Hermite polynomials. Accordingly, the approximation of the aggregated fluid–structure interaction (FSI) problem consists of an finite-element/boundary-element (FE/BE) coupled discretization. Contiguous use of finite-element/boundary-element (FE/BE) methods to exploit the advantages of both approaches, is an established practice; for a review see [43,31]. Applications include blood flow [38], elasto-plasticity [13], crack propagation [28] and electromagnetics [32], among others. Coupled finite-element/boundary-element (FE/BE) approaches have also been applied to fluid–structure interaction (FSI) problems in, e.g., [11,4,5,9], but the application of finite-element/boundary-element (FE/BE) has so far been restricted to fluid–structure interaction (FSI) problems with small deformations. The novelty of the present contribution lies in the exploitation of the boundary integral formulation in a new manner, viz., to enable very large deformations.

The remainder of this paper is organized as follows. Section 2 contains a statement of the considered fluid-membrane-interaction problem. Section 3 presents details of the discrete approximations and of the iterative solution procedure for the aggregated fluid–structure interaction (FSI) problem with contact. In Section 4, numerical experiments are conducted to exemplify the properties of the boundary element method (BEM) for fluid-membrane-interaction problems with large displacements. Finally, Section 5 presents concluding remarks.

2. Problem statement

In this section, the mathematical formulation of the considered fluid–structure interaction (FSI) problem with contact is presented. Section 2.1 considers the boundary-integral formulation for the fluid subproblem, consisting of an irrotational, incompressible flow. Section 2.2 is concerned with the structure subproblem. The interface conditions which provide for the connection between the fluid and the structure are specified in Section 2.3.

2.1. Boundary-integral formulation of the fluid subproblem

Consider a time-dependent open bounded domain $\Omega_t \subset \mathbb{R}^2$ with almost everywhere C^1 continuous boundary $\partial\Omega_t$. The boundary consists of the disjoint union of the time-dependent wet boundary Γ_t and the fixed inflow boundary Γ_{in}. It is assumed that the initial configuration of the boundary is specified by means of an arc-length parametrization conforming to:

$$\begin{aligned}\Gamma_0 &= \{\boldsymbol{x} \in \mathbb{R}^2 : \boldsymbol{x} = \boldsymbol{\chi}_0(s), s \in (0, L)\},\\ \Gamma_{\text{in}} &= \{\boldsymbol{x} \in \mathbb{R}^2 : \boldsymbol{x} = \boldsymbol{\chi}_0(s), s \in (L, \Lambda)\},\end{aligned} \tag{1}$$

with $|D\boldsymbol{\chi}_0(s)| = 1, |\cdot|$ the euclidean norm and D the (distributional) derivative $D\boldsymbol{z} = \partial\boldsymbol{z}/\partial s$. The configuration of the boundary is denoted by $\boldsymbol{z} : (0,T) \times (0,L) \to \mathbb{R}^2$, such that $\boldsymbol{z}(t,s)$ is the position at time t, of the material point initially at $\boldsymbol{\chi}_0(s)$. The condensed notation $\boldsymbol{z}_t$ denotes the configuration at specified time t. The boundary at time t is thus parametrized with respect to the arc length of the initial configuration according to $\partial\Omega_t = \{\boldsymbol{x} \in \mathbb{R}^2 : \boldsymbol{x} = \boldsymbol{z}_t(s), s \in (0, \Lambda)\}$; see Fig. 1 for an illustration. Because the inflow boundary is fixed, must hold that $\boldsymbol{z}_t(s) = \boldsymbol{\chi}_0(s)$ for $s \in \{L, \Lambda\}$.

The fluid subproblem consists of the irrotational flow of an incompressible fluid on the time-dependent domain Ω_t. Accordingly, there exists a harmonic potential $\phi : \Omega_t \to \mathbb{R}$ such that the fluid velocity $\boldsymbol{v}$ coincides with $\nabla\phi$. The wetted boundary Γ_t corresponds to a material boundary of the fluid domain, which implies that the normal velocity of the fluid coincides with the velocity of the boundary in its normal direction. Moreover, on the inflow boundary Γ_{in}, a normal velocity is prescribed. The boundary conditions for the fluid translate into Neumann-type conditions for the

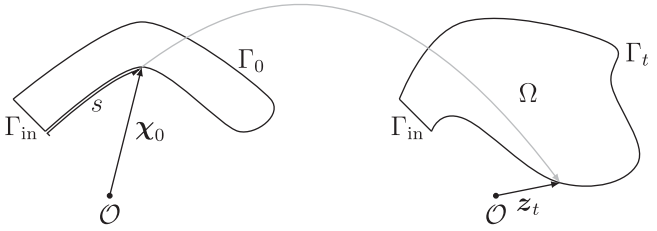

Fig. 1. Schematized problem geometry.

potential. The fluid is therefore described by the Laplace–Neumann problem:

$$-\Delta\phi = 0 \quad \text{in } \Omega_t, \tag{2a}$$

$$\partial_{\boldsymbol{n}}\phi = h \quad \text{on } \partial\Omega_t, \tag{2b}$$

where Δ denotes the Laplace operator and $h : \partial\Omega_t \to \mathbb{R}$ represents time-dependent exogenous data. To connect the fluid to the structure in the aggregated fluid–structure interaction (FSI) problem, only the trace of ϕ on $\partial\Omega_t$ is required. It is to be noted that (2) complies with a Fredholm alternative: existence of a solution to (2) is contingent on the condition that $\oint h = 0$, and the solution is unique only up to a constant; see also Section 2.4.

Given the structure of (2) and the restricted interest in the trace of ϕ, the Laplace–Neumann problem can be cast into a boundary-integral formulation. Various formulations of this type exist, viz., the direct formulation, and single-layer and double-layer formulations; see for instance [8]. To facilitate the connection with the membrane in the aggregated fluid–structure interaction (FSI) problem, the following direct formulation is most suitable:

$$\phi/2 + K\phi = Vh \quad \text{on } \partial\Omega_t, \tag{3}$$

where explicit use has been made of the assumed smoothness of $\partial\Omega_t$. The operators $K(\cdot)$ and $V(\cdot)$, generally referred to as the *single-layer potential* and the *double-layer potential*, respectively, correspond to (traces of) convolutions with singular kernels:

$$(Vh)(\boldsymbol{x}) := \oint_{\partial\Omega_t} G(\boldsymbol{x},\boldsymbol{y})\, h(\boldsymbol{y})\, d\sigma_t(\boldsymbol{y}), \tag{4a}$$

$$(K\phi)(\boldsymbol{x}) := \oint_{\partial\Omega_t} \partial_{\boldsymbol{n}} G(\boldsymbol{x},\boldsymbol{y})\, \phi(\boldsymbol{y})\, d\sigma_t(\boldsymbol{y}), \tag{4b}$$

where G denotes the Green's function for the negative Laplace operator in $\mathbb{R}^2$,

$$G(\boldsymbol{x},\boldsymbol{y}) := -(2\pi)^{-1} \log|\boldsymbol{x}-\boldsymbol{y}|, \tag{5}$$

and $d\sigma_t$ denotes the measure carried by the boundary $\partial\Omega_t$. Moreover, $\partial_{\boldsymbol{n}} G(\boldsymbol{x},\boldsymbol{y})$ stands for the conormal derivative of the Green's function with respect to its second argument:

$$\partial_{\boldsymbol{n}} G(\boldsymbol{x},\boldsymbol{y}) := (2\pi)^{-1} |\boldsymbol{x}-\boldsymbol{y}|^{-2} (\boldsymbol{x}-\boldsymbol{y}) \cdot \boldsymbol{n}(\boldsymbol{y}). \tag{6}$$

The double-layer potential is to be understood in the *Cauchy-principal-value* sense; see, e.g., [26,19,30]. A derivation of the above boundary-integral form of (2) can be found in, for instance, Refs. [22,40].

To enable a more precise interpretation of (3), denote by $H^1(\Omega_t)$ the Sobolev space of square-integrable functions with square-integrable distributional derivatives, by $H^{1/2}(\partial\Omega_t)$ the image of the trace operator on $H^1(\Omega_t)$, and by $H^{-1/2}(\partial\Omega_t)$ the dual space of $H^{1/2}(\partial\Omega_t)$. Note that the space $H^1(\Omega_t)$, and its trace and the dual thereof, are well defined whenever Ω_t corresponds to a Lipschitz transformation of a fixed Lipschitz domain, because H^1 is invariant with respect to such transformations. The data h in (2) corresponds to an element of $H^{-1/2}(\partial\Omega_t)$. The function ϕ in the left-hand side of (3) is the trace of a function in $H^1(\Omega_t)$ and, accordingly, it resides in $H^{1/2}(\partial\Omega_t)$. An important result due to Costabel [7, Theorem 1] is that the single-layer potential $V : H^{-1/2}(\partial\Omega_t) \to H^{1/2}(\partial\Omega_t)$ and the double-layer potential $K : H^{1/2}(\partial\Omega_t) \to H^{1/2}(\partial\Omega_t)$ are continuous mappings. Hence, Eq. (3) can be conceived of as an identity of elements in $H^{1/2}(\partial\Omega_t)$.

The Fredholm alternative that holds for the Laplace–Neumann problem (2) also applies to the boundary-integral formulation (3), as $1/2 + K$ has a nontrivial kernel consisting of constant functions and the image of $1/2 + K$ does not contain constant functions other than 0; cf. [36, Appendix B], for further details. A weak formulation of (3) is considered, in which the constant functions are removed from the test and trial spaces. Let $L^2(\partial\Omega_t)$ denote the Hilbert space of real-valued square-integrable functions on $\partial\Omega_t$, equipped with the inner product $(\phi,\psi)_{L^2(\partial\Omega_t)} = \oint_{\partial\Omega_t} \phi\psi$. The inner product $(\cdot,\cdot)_{L^2(\partial\Omega_t)}$ extends by continuity to a duality pairing on $H^{1/2}(\partial\Omega_t) \times H^{-1/2}(\partial\Omega_t)$ or $H^{-1/2}(\partial\Omega_t) \times H^{1/2}(\partial\Omega_t)$. Denoting by $H^{\pm1/2}_{\oint=0}(\partial\Omega_t) := \{\psi \in H^{\pm1/2}(\partial\Omega_t) : (\psi,1)_{L^2(\partial\Omega_t)} = 0\}$ the class of distributions in $H^{\pm1/2}(\partial\Omega_t)$ orthogonal to constants, the boundary-integral formulation (3) can be cast into the weak form:

$$\text{find } \phi \in H^{1/2}_{\oint=0}(\partial\Omega_t): \quad a_{\mathrm{f}}(\phi,\psi) = b_{\mathrm{f}}(\psi) \quad \forall\psi \in H^{-1/2}_{\oint=0}(\partial\Omega_t), \tag{7}$$

where the bilinear form $a_{\mathrm{f}} : H^{1/2}(\partial\Omega_t) \times H^{-1/2}(\partial\Omega_t) \to \mathbb{R}$ and the linear form $b_{\mathrm{f}} : H^{-1/2}(\partial\Omega_t) \to \mathbb{R}$ are defined by:

$$a_{\mathrm{f}}(\phi,\psi) = \left(\frac{1}{2}\phi + K\phi, \psi\right)_{L^2(\partial\Omega_t)}, \quad b_{\mathrm{f}}(\psi) = (Vh,\psi)_{L^2(\partial\Omega_t)}. \tag{8}$$

The bilinear form $a_{\mathrm{f}}(\cdot,\cdot)$ and linear form $b_{\mathrm{f}}(\cdot)$ according to (8) are continuous. From [30, Theorems 3.8.7 and 3.8.9] it moreover follows that:

$$C_K \|\phi\|_{H^{1/2}(\partial\Omega_t)} \leqslant \left\|\frac{1}{2}\phi + K\phi\right\|_{H^{1/2}(\partial\Omega_t)} \quad \forall\phi \in H^{1/2}_{\oint=0}(\partial\Omega_t), \tag{9a}$$

$$C_K \|\psi\|_{H^{-1/2}(\partial\Omega_t)} \leqslant \left\|\frac{1}{2}\psi + K'\psi\right\|_{H^{-1/2}\partial\Omega_t)} \quad \forall\psi \in H^{-1/2}_{\oint=0}(\partial\Omega_t), \tag{9b}$$

with $K' : H^{-1/2}(\partial\Omega_t) \to H^{-1/2}(\partial\Omega_t)$ the dual operator corresponding to K, and C_K a positive constant. These lower bounds on the norms of $1/2 + K$ and $1/2 + K'$ imply that the bilinear form $a_{\mathrm{f}}(\cdot,\cdot)$ satisfies:

$$\inf_{\phi\in H^{1/2}_{\oint=0}(\partial\Omega_t)\setminus\{0\}} \sup_{\psi\in H^{-1/2}_{\oint=0}(\partial\Omega_t)\setminus\{0\}} \frac{|a_{\mathrm{f}}(\phi,\psi)|}{\|\phi\|_{H^{1/2}(\partial\Omega_t)}\|\psi\|_{H^{-1/2}(\partial\Omega_t)}} \geqslant C_{\mathrm{f}} > 0, \tag{10a}$$

$$\forall\psi \in H^{-1/2}_{\oint=0}(\partial\Omega_t) \setminus \{0\} : \sup_{\phi\in H^{1/2}_{\oint=0}(\partial\Omega_t)\setminus\{0\}} |a_{\mathrm{f}}(\phi,\psi)| > 0, \tag{10b}$$

for some constant C_{f}. The bilinear form and the linear form therefore comply with the conditions of the Banach–Nečas–Babuška (BNB) theorem [14, Theorem 2.6], which implies that there exists a unique and stable solution to (7).

Although $H^{1/2}_{\oint=0}(\partial\Omega_t) \times H^{-1/2}_{\oint=0}(\partial\Omega_t)$ is the natural setting of the weak formulation of the boundary-integral formulation, in view of the connection to the underlying Laplace–Neumann problem, an alternative weak formulation in $L^2_{\oint=0}(\partial\Omega_t) = \{\phi \in L^2(\partial\Omega_t) : (\phi,1)_{L^2(\partial\Omega_t)} = 0\}$ can be established. Theorem 1 in [7] (see also [30, Section 3.1.2]) asserts, more precisely, that $K : H^{1/2+\varsigma}(\partial\Omega_t) \to H^{1/2+\varsigma}(\partial\Omega_t)$ is a continuous linear operator for any $\varsigma \in [-1/2, 1/2]$. Therefore, (7) can be conceived of as a weak formulation on $L^2_{\oint=0}(\partial\Omega_t) \times L^2_{\oint=0}(\partial\Omega_t)$,

$$\text{find } \phi \in L^2_{\oint=0}(\partial\Omega_t): \quad a_{\mathrm{f}}(\phi,\psi) = b_{\mathrm{f}}(\psi) \quad \forall\psi \in L^2_{\oint=0}(\partial\Omega_t), \tag{11}$$

if, accordingly, the bilinear form $(\cdot,\cdot)_{L^2(\partial\Omega_t)}$ in the definition of a_{f} and b_{f} in (8) is interpreted as a standard L^2 inner product, and not the extension to a duality pairing; see also [30, Section 3.8]. The BNB conditions (10) must then also be assessed with respect to $L^2_{\oint=0}(\partial\Omega_t)$.

Regarding Galerkin finite-element discretizations of (7) or (11), it is to be noted that standard conforming discretizations of the two formulations can be distinct, as discretizations of (7) have to be $H^{1/2}(\partial\Omega_t)$ conforming, while discretizations of (11) only have to be $L^2(\partial\Omega_t)$ conforming. For instance, a conforming approximation to (7) would have to be continuous, while a conforming

approximation to (11) does not. Approximations of (7) and (11) based on $H^{1/2}(\partial\Omega_t)$-conforming finite-element spaces are evidently identical.

Moreover, to further facilitate the implementation, the orthogonality condition $(\cdot,1)_{L^2(\partial\Omega_t)}=0$ is removed from the test- and trial-spaces and instead impose it by means of Lagrange multipliers.

2.2. Structure subproblem

The wet boundary of the fluid is composed of a membrane corresponding to a regularized linearly-elastic string:

$$\boldsymbol{z}''-D\Big(D\boldsymbol{z}(1-|D\boldsymbol{z}|^{-1})\Big)+\epsilon D^4\boldsymbol{z}=\boldsymbol{f}\quad\text{on }(0,T)\times(0,L),\tag{12}$$

where $(\cdot)'$ denotes the time derivative. Recall that $\boldsymbol{z}(t,s)$ governs the current position of the boundary $\partial\Omega_t$. The load $\boldsymbol{f}$ depends implicitly on $\boldsymbol{z}$ due to contact forces and fluid loads; see Eq. (15) below. The first two terms in the left-hand side of (12) correspond to a linearly-elastic string. The final term yields a regularization, which is required to avoid instability in compression, i.e., when $|D\boldsymbol{z}|\leqslant 1$. The string equation in (12) can be derived from the general equations of motion of an elastic solid under the assumptions of linestress and linear elasticity and, in particular, the strain term corresponds to a strain energy $\Psi=E+1-\sqrt{2E+1}$ with $E=(|D\boldsymbol{z}|^2-1)/2$ the Green–Lagrange strain tensor. Eq. (12) is in fact in nondimensional form. The nondimensionalization is elaborated in Appendix A.

Eq. (12) must be complemented with suitable initial and boundary conditions. The membrane is attached to hinged supports, which fix the position of the membrane without inducing moments:

$$\boldsymbol{z}(t,s)=\boldsymbol{\chi}_0(s),\quad D^2\boldsymbol{z}(t,s)=0\quad\text{for } s\in\{0,L\}\text{ and } t\in(0,T).\tag{13}$$

The initial conditions on the position of the membrane are provided by

$$\boldsymbol{z}(0,\cdot)=\boldsymbol{\chi}_0(\cdot),\quad \boldsymbol{z}'(0,\cdot)=\boldsymbol{\chi}_1(\cdot),\tag{14}$$

where $\boldsymbol{\chi}_0$ refers to the initial configuration and $\boldsymbol{\chi}_1$ represents a prescribed initial velocity.

The load on the membrane consists of the fluid traction, proportional to pressure p, and the contact force. The fluid traction induces a load in the normal direction of the membrane. The contact force is represented by a nonlinear operator, $\boldsymbol{\varphi}_{\boldsymbol{z}}$, which associates to any configuration a load on that configuration; see Section 2.5. The load $\boldsymbol{f}$ can be separated into

$$\boldsymbol{f}:=|D\boldsymbol{z}|(p\circ\boldsymbol{z}\,\boldsymbol{n}_{\boldsymbol{z}}\circ\boldsymbol{z}+\boldsymbol{\varphi}_{\boldsymbol{z}}\circ\boldsymbol{z})=p\circ\boldsymbol{z}\,\mathrm{rot}\,D\boldsymbol{z}+|D\boldsymbol{z}|\boldsymbol{\varphi}_{\boldsymbol{z}}\circ\boldsymbol{z},\tag{15}$$

with $\mathrm{rot}:\mathbb{R}^2\to\mathbb{R}^2$ the rotation operator, $\mathrm{rot}\,(a_1,a_2)=(a_2,-a_1)$. It is to be noted that the normal vector depends explicitly on the configuration. The composition of $p,\boldsymbol{n}_{\boldsymbol{z}}$ and $\boldsymbol{\varphi}_{\boldsymbol{z}}$ with $\boldsymbol{z}$ serves to transport the pressure, the normal vector and the contact load to the parameterized interval $(0,L)$. The multiplication by $|D\boldsymbol{z}|$ accounts for the ratio of the surface measures in the initial and the actual configuration.

A more precise specification of (12)–(15) is now considered. To this end, some elementary notational conventions are required. Denote by $\boldsymbol{L}^p(0,L)$ $(1\leqslant p<\infty)$ the Lebesgue space of functions from $(0,L)$ into $\mathbb{R}^2$ with p-integrable Euclidean norm, equipped with the norm $\|\cdot\|_{\boldsymbol{L}^p(0,L)}=(\int_0^L|\cdot|^p)^{1/p}$. For $p=\infty$, the above definition is extended by setting $\|\boldsymbol{z}\|_{\boldsymbol{L}^\infty(0,L)}=\operatorname{ess\,sup}\{|\boldsymbol{z}(s)|:s\in(0,L)\}$. Furthermore, denote by $\boldsymbol{W}^{m,p}(0,L)$ the Sobolev space of functions $\boldsymbol{z}\in\boldsymbol{L}^p(0,L)$ with distributional derivatives $D^k\boldsymbol{z}\in\boldsymbol{L}^p(0,L)$ for all $k\leqslant m$. The spaces $\boldsymbol{L}^2(0,L)$ and $\boldsymbol{H}^m(0,L):=\boldsymbol{W}^{m,2}(0,L)$ $(m\in\mathbb{Z}_+)$ are Hilbert spaces when provided with the inner products

$$(\boldsymbol{w},\boldsymbol{z})_{\boldsymbol{L}^2(0,L)}=\int_0^L\boldsymbol{w}(s)\cdot\boldsymbol{z}(s)\,ds,\quad(\boldsymbol{w},\boldsymbol{z})_{\boldsymbol{H}^2(0,L)}$$
$$=(\boldsymbol{w},\boldsymbol{z})_{\boldsymbol{L}^2(0,L)}+\sum_{k=1}^{2}(D^k\boldsymbol{w},D^k\boldsymbol{z})_{\boldsymbol{L}^2(0,L)}.$$

The subspace of $\boldsymbol{H}^m(0,L)$ $(m\in\mathbb{N})$ of functions that vanish on the boundary $\{0,L\}$ is denoted $\boldsymbol{H}_0^m(0,L)$, which, for notational convenience, deviates from the standard notation $\boldsymbol{H}^m(0,L)\cap\boldsymbol{H}_0^1(0,L)$. Considering a time interval $(0,T)$ and a normed space $(\boldsymbol{B},\|\cdot\|_{\boldsymbol{B}})$, denote by $L^q(0,T;\boldsymbol{B})$ $(1\leqslant q<\infty)$ the Bochner space of functions $\boldsymbol{z}:(0,T)\to\boldsymbol{B}$ such that the function $t\mapsto\|\boldsymbol{z}(t)\|_{\boldsymbol{B}}$ is q-integrable, equipped with the norm $\|\boldsymbol{z}\|_{L^q(0,T;\boldsymbol{B})}=(\int_0^T\|\boldsymbol{z}(t)\|_{\boldsymbol{B}}^q\,dt)^{1/q}$. These definitions are extended to $q=\infty$ by setting $\|\boldsymbol{z}\|_{L^\infty(0,T;\boldsymbol{B})}=\operatorname{ess\,sup}\{\|\boldsymbol{z}(t)\|_{\boldsymbol{B}}:t\in(0,T)\}$.

On account of the nonlinear dependence of the stress $(1-|D\boldsymbol{z}|^{-1})$ and of the load vector $\boldsymbol{f}$ in (15) on $\boldsymbol{z}$, a precise specification of the domain of the structure operator is nontrivial. The principal part of the operator, corresponding to the regularizing term $\epsilon D^4(\cdot)$, is however linear and elliptic. Assume now that the character of the principal part extends to the nonlinear structure operator. Restricting considerations to the principal part of the structure operator, Eq. (12) corresponds to an evolution equation of the second order (in t) with an elliptic operator ϵD^4 from $\boldsymbol{H}_0^2(0,L)$ into its dual space $\boldsymbol{H}^{-2}(0,L)$. A comprehensive general theory is available for evolution equations of this type; see, for instance, [10,15,23]. Ignoring the nonlinear term in (12), and insisting that $\boldsymbol{\chi}_0\in\boldsymbol{H}_0^2(0,L)$ and $\boldsymbol{\chi}_1\in\boldsymbol{L}^2(0,L)$, Eq. (12) subject to (13) and (14) defines a unique solution in $\boldsymbol{\chi}_0+W(0,T)$ for all $\boldsymbol{f}\in L^2(0,T;\boldsymbol{L}^2(0,L))$, with $W(0,T)$ the collection of admissible structure displacements:

$$W(0,T)=\Big\{\boldsymbol{w}\in L^2\Big(0,T;\boldsymbol{H}_0^2(0,L)\Big):\boldsymbol{w}'\in L^2\Big(0,T;\boldsymbol{L}^2(0,L)\Big)\Big\}.\tag{16}$$

Moreover, it holds that $\boldsymbol{z}''\in L^2(0,T;\boldsymbol{H}^{-2}(0,L))$.

It is assumed that the setting of the structural position in (16) can be retained for the nonlinear operator. In addition, it is assumed that $|D\boldsymbol{z}|$ is a.e. bounded from below, i.e.,

$$|D\boldsymbol{z}|\geqslant\alpha>0,\quad s\in(0,L),\tag{17}$$

and that $\boldsymbol{z}(t,\cdot):(0,L)\to\Gamma_t$ is bijective for all $t\in(0,T)$. The first assumption reflects that parts of the membrane that initially have finite extent do not vanish during the motion. The second assumption prohibits self-intersection of the membrane.

The general theory for evolution equations of the second order in [23, Section 3.8.4] provides a refined regularity result for the solution to (12)–(14). Under the above conditions on the data, the displacement and the velocity can be conceived of as continuous-in-time functions, taking values in $\boldsymbol{H}_0^2(0,L)$ and $\boldsymbol{L}^2(0,L)$, respectively, and the solution to (12)–(14) in fact satisfies

$$\boldsymbol{z}\in\boldsymbol{\chi}_0+\Big\{\boldsymbol{w}\in L^\infty\Big(0,T;\boldsymbol{H}_0^2(0,L)\Big):\boldsymbol{w}'\in L^\infty\Big(0,T;\boldsymbol{L}^2(0,L)\Big)\Big\}.\tag{18}$$

This refined regularity result is important to assign significance to the transmission conditions in the aggregated fluid–structure interaction (FSI) problem; see Section 2.3.

It is to be remarked that the above elementary model for a membrane is in fact surprizingly difficult to analyze. Refs. [41,1] derive the model (without regularization) without regard for the complications related to compression. Results on existence and uniqueness appear to be nonexistent; see also [2].

2.3. Transmission conditions

The fluid and the structure interact at their mutual interface via so-called transmission conditions. These transmission conditions can be separated into a dynamic condition, which specifies continuity of tractions, and a kinematic condition, which expresses continuity of motion. The kinematic condition imposes that on the wetted boundary Γ_t, the normal velocity of the fluid coincides with the normal velocity of the membrane. Indicating the normal velocity on the inflow boundary Γ_{in} by q, the kinematic condition translates into the following specification of the Neumann data h in (2):

$$h = \begin{cases} \boldsymbol{n}_{\boldsymbol{z}_t} \cdot (\boldsymbol{z}'_t \circ \boldsymbol{z}_t^{-1}) & \text{at } \Gamma_t, \\ q & \text{at } \Gamma_{\text{in}}. \end{cases} \tag{19}$$

The composition of $\boldsymbol{z}'_t$ with $\boldsymbol{z}_t^{-1}$ serves to transport $\boldsymbol{z}'_t$ to Γ_t.

The dynamic condition imposes continuity of tractions at the fluid–structure interface. The pressure can be extracted from Bernoulli's principle. Considering only quasi-static flows, allows to suppress the time-dependence of the potential in Bernoulli's relation, it follows that the pressure p in the structure load according to (15) is related to the flow potential by:

$$\begin{aligned} p(\phi) &:= p_0 - \frac{1}{2}\vartheta|\nabla\phi|^2 = p_0 - \frac{1}{2}\vartheta|\partial_{\boldsymbol{n}}\phi|^2 - \frac{1}{2}\vartheta|\nabla_\Gamma\phi|^2 \\ &= p_0 - \frac{1}{2}\vartheta(\boldsymbol{n}_{\boldsymbol{z}} \cdot (\boldsymbol{z}' \circ \boldsymbol{z}^{-1}))^2 + \frac{1}{2}\vartheta|\nabla_\Gamma\phi|^2, \end{aligned} \tag{20}$$

with ϑ the fluid–structure mass ratio. The second equality follows from splitting the gradient into normal and tangential components respectively. The normal component is the Neumann data provided in (19). In the tangential component, the symbol ∇_Γ denotes the so-called *tangential gradient* (or Γ-*gradient*), formally, $\nabla_\Gamma\phi = \nabla\phi - \boldsymbol{n}\partial_{\boldsymbol{n}}\phi$. Moreover, p_0 represents a (possibly time-dependent) pressure level; cf. Section 2.4.

To be compatible with the domain of the single-layer potential, the Neumann data (19) in accordance with the kinematic condition must reside in $L^q(0,T;H^{-1/2}(\partial\Omega_t))$ $(1 \leqslant q \leqslant \infty)$. The time-dependence of the Neumann data then extends to the solution of the boundary-integral formulation and $\phi \in L^q(0,T;H^{1/2}(\partial\Omega_t))$. By transporting the integral on Γ_t to the parameter interval $(0,L)$ and, subsequently, applying Hölder's inequality, it is inferred that:

$$\begin{aligned} \|h\|_{L^\infty(0,T;L^2(\Gamma_t))} &= \left\| \left(\int_{\Gamma_t} \left(\boldsymbol{n}_{\boldsymbol{z}}(\cdot,\boldsymbol{x}) \cdot \boldsymbol{z}' \circ \boldsymbol{z}^{-1}(\cdot,\boldsymbol{x})\right)^2 d\sigma_t \right)^{1/2} \right\|_{L^\infty(0,T)} \\ &\leqslant \left\| \left(\int_0^L |\boldsymbol{n}_{\boldsymbol{z}} \circ \boldsymbol{z}(\cdot,s)|^2 |\boldsymbol{z}'(\cdot,s)|^2 |D\boldsymbol{z}(\cdot,s)|\, ds \right)^{1/2} \right\|_{L^\infty(0,T)} \\ &\leqslant \|\boldsymbol{z}'\|_{L^\infty(0,T;\boldsymbol{L}^2(0,L))} \|D\boldsymbol{z}\|^{1/2}_{L^\infty(0,T;\boldsymbol{L}^\infty(0,L))}. \end{aligned} \tag{21}$$

In the final inequality it has been taken into account that $|D\boldsymbol{z}|^{-1}|\text{rot}\, D\boldsymbol{z}| \leqslant 1$ almost everywhere. Sobolev's inequality (cf. for instance [3, Theorem 1.4.6]) implies that the embedding $\boldsymbol{H}^1(0,L) \hookrightarrow \boldsymbol{L}^\infty(0,L)$ is continuous. The refined regularity result (18) then leads to the conclusion that $\|h\|_{L^\infty(0,T;L^2(\Gamma_t))}$ is bounded. Assuming that the inflow data satisfies $q \in L^\infty(0,T;L^2(\Gamma_{\text{in}}))$, it can be shown that $h \in L^\infty(0,T;L^2(\partial\Omega_t))$ and, a fortiori, it holds that h defines a functional in $L^\infty(0,T;H^{-1/2}(\partial\Omega_t))$. The refined regularity result in [7, Theorem 3] in fact conveys that the increased regularity of the Neumann data, viz., $h \in L^\infty(0,T;L^2(\partial\Omega_t))$ rather than $h \in L^\infty(0,T;H^{-1/2}(\partial\Omega_t))$, carries over to the solution of the boundary-integral formulation and results in $\phi \in L^\infty(0,T;H^1(\partial\Omega_t))$ instead of $\phi \in L^\infty(0,T;H^{1/2}(\partial\Omega_t))$.

Dynamic equilibrium at the fluid–structure interface imposes that the fluid exerts a load $p\boldsymbol{n}_{\boldsymbol{z}}$ on the structure, with p according to Bernoulli's relation (20). The standard setting of the structure subproblem therefore insists on $(p\boldsymbol{n}_{\boldsymbol{z}}) \circ \boldsymbol{z} \in L^2(0,T;\boldsymbol{L}^2(0,L))$; see Section 2.2. A result of this type however requires more regularity for $\boldsymbol{z}$ and $\nabla_\Gamma\phi$. We shall therefore consider the weaker result $(p\boldsymbol{n}_{\boldsymbol{z}}) \circ \boldsymbol{z} \in L^2(0,T;\boldsymbol{H}^{-2}(0,L))$, which is consistent with the interpretation of (12) as an identity in $L^2(0,T;\boldsymbol{H}^{-2}(0,L))$. To this end, it will be shown that the map

$$\boldsymbol{w} \mapsto \int_0^T \int_0^L \boldsymbol{w}(t,s) \cdot (p \circ \boldsymbol{z}(t,s)\, \text{rot}\, D\boldsymbol{z}(t,s))\, ds\, dt \tag{22}$$

with p according to Bernoulli's relation (20), corresponds to a continuous linear functional on $L^2(0,T;\boldsymbol{H}^2_0(0,L))$; cf. (15). Without loss of generality, ϑ is set to 1. Application of Hölder's inequality to the term corresponding to the pressure level p_0 yields:

$$\begin{aligned} &\left| \int_0^T \int_0^L p_0(t)\, \boldsymbol{w}(t,s) \cdot \text{rot}\, D\boldsymbol{z}(t,s)\, ds\, dt \right| \\ &\quad \leqslant \|p_0\|_{L^2(0,T)} \|\boldsymbol{w}\|_{L^2(0,T;\boldsymbol{L}^2(0,L))} \|D\boldsymbol{z}\|_{L^\infty(0,T;\boldsymbol{L}^2(0,L))}. \end{aligned}$$

Anticipating that the pressure level p_0 resides in $L^2(0,T)$ (see Section 2.4) and and recalling the refined regularity result (18), the p_0-term is therefore indeed continuous. Hölder's inequality implies that the term corresponding to $(\partial_{\boldsymbol{n}}\phi)^2$ in (20) is bounded according to

$$\begin{aligned} &\left| \int_0^T \int_0^L \boldsymbol{w}(t,s) \cdot \text{rot}\, D\boldsymbol{z}(t,s) (\boldsymbol{z}'(t,s) \cdot \boldsymbol{n}_{\boldsymbol{z}} \circ \boldsymbol{z}(t,s))^2\, ds\, dt \right| \\ &\quad \leqslant \int_0^T \|\boldsymbol{w}(t,\cdot)\|_{\boldsymbol{L}^\infty(0,L)} \|D\boldsymbol{z}(t,\cdot)\|_{\boldsymbol{L}^\infty(0,L)} \|\boldsymbol{z}'(t,\cdot)\|^2_{\boldsymbol{L}^2(0,L)} dt \\ &\quad \leqslant \|\boldsymbol{w}\|_{L^2(0,T;\boldsymbol{L}^\infty(0,L))} \|D\boldsymbol{z}\|_{L^\infty(0,T;\boldsymbol{L}^\infty(0,L))} \|\boldsymbol{z}'\|^2_{L^\infty(0,T;\boldsymbol{L}^2(0,L))}, \end{aligned}$$

Note that the first inequality takes into account that $|\boldsymbol{n}_{\boldsymbol{z}}| \leqslant 1$ almost everywhere. The refined regularity result (18) and the continuity of the embedding $\boldsymbol{H}^m(0,L) \hookrightarrow \boldsymbol{L}^\infty(0,L)$ $(m \in \mathbb{N})$ then conveys that the term related to $(\partial_{\boldsymbol{n}}\phi)^2$ is indeed bounded. Hence, it remains to bound the term originating from the surface gradient in Bernoulli's relation. Hölder's inequality yields:

$$\begin{aligned} &\left| \int_0^T \int_0^L \boldsymbol{w}(t,s) \cdot \text{rot}\, D\boldsymbol{z}(t,s)\, (\nabla_\Gamma\phi)^2 \circ \boldsymbol{z}(t,s)\, ds\, dt \right| \\ &\quad \leqslant \|\boldsymbol{w}\|_{L^2(0,T;\boldsymbol{L}^\infty(0,L))} \|D\boldsymbol{z}\|_{L^\infty(0,T;\boldsymbol{L}^\infty(0,L))} \|\nabla_\Gamma\phi \circ \boldsymbol{z}\|^2_{L^4(0,T;\boldsymbol{L}^2(0,L))}. \end{aligned}$$

Boundedness of the first two factors in the right-hand side again follows from the refined regularity result (18) and the aforementioned embedding relation. Boundedness of the right-most factor follows straightforwardly from the lower bound (17) on $|D\boldsymbol{z}|$ and the refined regularity result $\phi \in L^2(0,T;\boldsymbol{H}^1(\partial\Omega_t))$.

2.4. Compatibility condition

The selection of the pressure level p_0 is not obvious. The pressure level is in fact related to an auxiliary coupling condition between the fluid and the structure, in addition to the aforementioned kinematic and dynamic interface conditions, which originates from the incompressibility of the fluid. The incompressibility of the fluid engenders a Fredholm alternative for the Laplace–Neumann problem (2). By the divergence theorem, the identities are obtained:

$$\int_{\Omega_t} \Delta\phi = \oint_{\partial\Omega_t} \partial_{\boldsymbol{n}}\phi = \oint_{\partial\Omega_t} h = 0. \tag{23}$$

Hence, the Laplace–Neumann problem admits a solution if and only if the data h complies with the compatibility condition $\oint h = 0$. Moreover, $\ker(\Delta, \partial_{\boldsymbol{n}}) = \text{span}\{1\}$ and, hence, the solution to (2) is unique only up to an additive constant. On account of (19), the compatibility condition in (23) translates into a compatibility condition on the structure displacement. Such an auxiliary coupling between the fluid and the structure is typical for fluid–structure interaction (FSI) problems with enclosed incompressible fluids; see also [21].

Denoting by $Q(\boldsymbol{z}_t)$ the volume contained within a certain structure configuration $\boldsymbol{z}_t$ and by $c(t)$ the content of the fluid domain,

$$c(t) = Q(\boldsymbol{\chi}_0) + \int_0^t \int_{\Gamma_{\text{in}}} q, \tag{24}$$

the structure displacement must comply with $Q(\boldsymbol{z}_t) = c(t)$. This compatibility condition is now imposed in the weak formulation of (12)–(14) by means of a Lagrange multiplier. Moreover, to elucidate the relation between the pressure level, p_0, and the compatibility condition, $\boldsymbol{f}$ in (12) is separated in accordance with (15) and, subsequently, p is replaced in accordance with (20). Denote by

$$W_0(0,T) = \{\boldsymbol{z} \in W(0,T); \boldsymbol{z}(0,\cdot) = 0\}, \tag{25a}$$

$$W_T(0,T) = \{\boldsymbol{z} \in W(0,T); \boldsymbol{z}(T,\cdot) = 0\}, \tag{25b}$$

the admissible structure-displacement fields with vanishing initial and terminal traces, respectively. It is to be remarked that the trace of $\boldsymbol{z}$ at $t = 0$ in (25a) is well defined in $\boldsymbol{L}^2(0,L)$; see, for instance, [23,15,14]. The structure-displacement problem, including the volume constraint, can then be condensed into the weak formulation:

find $\boldsymbol{z} \in \boldsymbol{\chi}_0 + W_0(0,T)$, $\lambda \in L^2(0,T)$ such that $\forall \boldsymbol{w} \in W_T(0,T)$, $\mu \in L^2(0,T)$:

$$\begin{aligned}
&-\int_0^T (\boldsymbol{z}'(t,\cdot), \boldsymbol{w}'(t,\cdot))_{\boldsymbol{L}^2(0,L)}\,dt + \int_0^T a_s(\boldsymbol{z}(t,\cdot); \boldsymbol{w}(t,\cdot))\,dt \\
&\quad - \int_0^T p_0(t)(\operatorname{rot} D\boldsymbol{z}(t,\cdot), \boldsymbol{w}(t,\cdot))_{\boldsymbol{L}^2(0,L)}\,dt \\
&\quad + \frac{\vartheta}{2}\int_0^T \langle |\nabla\phi|^2 \circ \boldsymbol{z}(t,\cdot) \operatorname{rot} D\boldsymbol{z}(t,\cdot), \boldsymbol{w}(t,\cdot)\rangle\,dt \\
&\quad - \int_0^T \langle |D\boldsymbol{z}(t,\cdot)|\, \boldsymbol{\varphi}_{\boldsymbol{z}} \circ \boldsymbol{z}(t,\cdot), \boldsymbol{w}(t,\cdot)\rangle\,dt \\
&\quad + \int_0^T \lambda(t)\,\langle \delta Q(\boldsymbol{z}(t,\cdot)), \boldsymbol{w}(t,\cdot)\rangle\,dt + \int_0^T \mu(t) Q(\boldsymbol{z}(t,\cdot))\,dt \\
&\quad = \int_0^T \mu(t)\,c(t)\,dt + (\boldsymbol{\chi}_1, \boldsymbol{w}(0,\cdot))_{\boldsymbol{L}^2(0,L)},
\end{aligned} \tag{26a}$$

where the semilinear form $a_s : \boldsymbol{H}^2(0,L) \times \boldsymbol{H}^2(0,L) \to \mathbb{R}$ is defined by

$$a_s(\boldsymbol{z};\boldsymbol{w}) = \Big((1 - |D\boldsymbol{z}|^{-1}) D\boldsymbol{z}, D\boldsymbol{w}\Big)_{\boldsymbol{L}^2(0,L)} + \epsilon\Big(D^2\boldsymbol{z}, D^2\boldsymbol{w}\Big)_{\boldsymbol{L}^2(0,L)} \tag{26b}$$

and $\langle\cdot,\cdot\rangle$ denotes the duality pairing between $\boldsymbol{H}^{-2}(0,L)$ and $\boldsymbol{H}_0^2(0,L)$. Moreover, $\delta Q : \boldsymbol{H}^2(0,L) \to \boldsymbol{H}^{-2}(0,L)$ denotes the Fréchet derivative of the volume functional Q.

In the weak formulation (26a), the pressure level p_0 can be identified with the Lagrange multiplier $\lambda \in L^2(0,T)$. More precisely, if $(\boldsymbol{z},\lambda)^0$ denotes the solution to (26a) for $p_0 = 0$ and by $(\boldsymbol{z},\lambda)^1$ the solution to (26a) for some arbitrary $p_0 \in L^2(0,T)$, then it holds that $\boldsymbol{z}^1 = \boldsymbol{z}^0$ and $\lambda^1 = \lambda^0 + p_0$. To prove this assertion, it will shown that

$$\langle \delta Q(\boldsymbol{z}(t,\cdot)), \boldsymbol{w}(t,\cdot)\rangle = (\operatorname{rot} D\boldsymbol{z}(t,\cdot), \boldsymbol{w}(t,\cdot))_{\boldsymbol{L}^2(0,L)}, \tag{27}$$

for all admissible structure configurations $\boldsymbol{z} \in \boldsymbol{\chi}_0 + W_0(0,T)$ and all $\boldsymbol{w} \in L^2(0,T;\boldsymbol{H}_0^2(0,L))$. The time-dependence of the structure configuration is in fact irrelevant in (27) and will be suppressed in the ensuing derivation. First, note that

$$\begin{aligned}
Q(\boldsymbol{z}) &= \int_{\Omega_t} d\boldsymbol{x} = \frac{1}{2}\int_{\Omega_t} \operatorname{div}\boldsymbol{x}\,d\boldsymbol{x} = \frac{1}{2}\oint_{\partial\Omega_t} \boldsymbol{x}\cdot\boldsymbol{n}\,d\sigma_t \\
&= \frac{1}{2}\int_0^\Lambda \boldsymbol{z}(s)\cdot\operatorname{rot} D\boldsymbol{z}(s)\,ds.
\end{aligned} \tag{28}$$

The penultimate expression in (28) is a straightforward consequence of the divergence theorem. The ultimate expression follows from the transformation $s \mapsto \boldsymbol{x} = \boldsymbol{z}(s)$. Consider an arbitrary $\boldsymbol{w} \in \boldsymbol{H}_0^2(0,L)$ and extend it to (L,Λ) by zero. The extension is still denoted by $\boldsymbol{w}$. From (28), it holds that:

$$\begin{aligned}
\langle \delta Q(\boldsymbol{z}), \boldsymbol{w}\rangle &:= \frac{d}{d\varepsilon} Q(\boldsymbol{z} + \varepsilon\boldsymbol{w})\Big|_{\varepsilon=0} \\
&= \frac{1}{2}(\operatorname{rot} D\boldsymbol{z}, \boldsymbol{w})_{\boldsymbol{L}^2(0,L)} + \frac{1}{2}(\boldsymbol{z}, \operatorname{rot} D\boldsymbol{w})_{\boldsymbol{L}^2(0,L)}.
\end{aligned} \tag{29}$$

It is easily verified that the right-hand side of (29) is linear in $\boldsymbol{z}$ and $\boldsymbol{w}$ and that

$$\left|\frac{1}{2}(\operatorname{rot} D\boldsymbol{z}, \boldsymbol{w})_{\boldsymbol{L}^2(0,L)} + \frac{1}{2}(\boldsymbol{z}, \operatorname{rot} D\boldsymbol{w})_{\boldsymbol{L}^2(0,L)}\right| \leqslant \|\boldsymbol{z}\|_{\boldsymbol{H}^2(0,L)} \|\boldsymbol{w}\|_{\boldsymbol{H}^2(0,L)}. \tag{30}$$

Hence, the Fréchet derivative $\delta Q(\cdot)$ can be identified with a linear continuous operator from $\boldsymbol{H}^2(0,L)$ into $\boldsymbol{H}^{-2}(0,L)$, and for each $\boldsymbol{z} \in \boldsymbol{H}^2(0,L)$ the duality pairing of $\delta Q(\boldsymbol{z})$ with $\boldsymbol{w} \in \boldsymbol{H}_0^2(0,L)$ is defined by the right-hand side of (29). The identity (27) is obtained by recasting the second term in the right-hand side of (29) into:

$$(\boldsymbol{z}, \operatorname{rot} D\boldsymbol{w})_{\boldsymbol{L}^2(0,L)} = -(\operatorname{rot}\boldsymbol{z}, D\boldsymbol{w})_{\boldsymbol{L}^2(0,L)} = (\operatorname{rot} D\boldsymbol{z}, \boldsymbol{w})_{\boldsymbol{L}^2(0,L)}. \tag{31}$$

The first identity in (31) is a consequence of the skew-symmetry of the rotation operator. The second identity follows from integration-by-parts and $\boldsymbol{w}|_{\{0,L\}} = 0$.

2.5. Contact forces

In the treatment of complex folded geometries, adequate modeling of self-contact of the membrane is imperative to avoid self-intersection. Because the primary interest concerns the coupled problem described in Sections 2.1–2.4 and, in this context, contact modeling is only accessory, any cogent contact model that prevents self-intersection is therefore satisfactory. For this reason, a soft-contact model is considered based on repulsive potentials, instead of a hard-contact model, as the latter requires contact detection, which is nontrivial. Moreover, the soft-contact model admits an efficient implementation by recycling the kernels that have already been generated in the boundary-element method for the fluid subproblem.

In the soft-contact model, each segment of the membrane exerts a force on every other segment, depending on their relative distance and orientation. The contact-induced traction on the structure, $\boldsymbol{z} \mapsto \boldsymbol{\varphi}_{\boldsymbol{z}}$, is modeled as the marginal of a vector-valued traction density, i.e., it is postulated that:

$$\boldsymbol{\varphi}_{\boldsymbol{z}}(\boldsymbol{x}) = \zeta \oint_{\partial\Omega} \boldsymbol{F}(\boldsymbol{x},\boldsymbol{y})\,d\sigma(\boldsymbol{y}), \tag{32}$$

for some traction density $\boldsymbol{F} : \partial\Omega \times \partial\Omega \to \mathbb{R}^2$, with $\zeta > 0$ a model parameter. Note that $\boldsymbol{\varphi}_{\boldsymbol{z}}$ depends implicitly on the structure configuration, $\boldsymbol{z}$, on account of the dependence of the domain Ω on $\boldsymbol{z}$. Moreover, assume that the inflow boundary Γ_{in} also exerts a contact traction. The time dependence of the structural configuration and of the domain are irrelevant for the exposition, and will be suppressed. The traction density should comply with the following elementary conditions:

- C1. The traction density should be essentially local, i.e., it should have local support or decay rapidly as the distance $|\boldsymbol{x} - \boldsymbol{y}|$ increases;
- C2. The traction density is repulsive and acts in the direction $\boldsymbol{x} - \boldsymbol{y}$ of the relative position of segments of the membrane;
- C3. The traction at any point induced by segments in the vicinity of that point vanishes. This means that for each $\boldsymbol{x} \in \partial\Omega$ and each $\varepsilon > 0$ there exist a $\delta > 0$ and a connected subset $\Gamma_\delta \subset \partial\Omega$ such that $\boldsymbol{x} \in \Gamma_\delta$ and
$$\frac{1}{\operatorname{meas}\Gamma_\delta}\left|\int_{\Gamma_\delta} \boldsymbol{F}(\boldsymbol{x},\boldsymbol{y})\,d\sigma(\boldsymbol{y})\right| < \varepsilon \tag{33}$$
with $\operatorname{meas}\Gamma_\delta$ the surface measure of Γ_δ;
- C4. The contact force should prevent self-intersection of the membrane. To this end, the traction density must approach infinity if $\boldsymbol{y} \to \boldsymbol{x}$ while $\boldsymbol{y}$ and $\boldsymbol{x}$ are separated on the membrane. In particular, if there exists a sequence $\{\boldsymbol{y}_n\} \subset \Gamma$, $\boldsymbol{y}_n \to \boldsymbol{x}$ as $n \to \infty$, a corresponding sequence of sections $\Gamma_n \subset \Gamma$,

$$\Gamma_n = \{\Gamma_n \text{ is the smallest connected subset of } \partial\Omega \text{ containing } \boldsymbol{x} \text{ and } \boldsymbol{y}_n\} \tag{34}$$

and a number $\varepsilon > 0$ such that $\operatorname{meas}\Gamma_n \geqslant \varepsilon$ as $n \to \infty$, then $|\boldsymbol{F}(\boldsymbol{x},\boldsymbol{y}_n)| \to \infty$ as $n \to \infty$; cf. also condition C3;

C5. The traction density should satisfy a reciprocity principle in accordance with Newton's third law of motion, which implies $\boldsymbol{F}(\boldsymbol{y},\boldsymbol{x}) = -\boldsymbol{F}(\boldsymbol{x},\boldsymbol{y})$.

An important observation pertains to the fact that, in the finite-element approximation, the concomitant computational complexity of the soft-contact model is proportional to the number of elements squared, as for each element all other elements are to be visited to determine the relative distances. In the present setting, however, the relative distances have already been computed in the boundary-integral formulation of the fluid subproblem. Moreover, it will be shown that the dependence of the contact force on the relative distance and orientation can be formulated such that the aforementioned conditions are obeyed, and that the traction density can be composed of the singular kernel in the double-layer potential in (4b). The authors are not aware of previous work on such recycling of discrete kernels of a boundary-integral formulation to determine contact forces.

To facilitate the presentation, the traction density is factorized in four components according to $\boldsymbol{F}(\boldsymbol{x},\boldsymbol{y}) = b(r/d)\, v(\boldsymbol{x},\boldsymbol{y})\, r^{-1}\boldsymbol{d}(\boldsymbol{x},\boldsymbol{y})$, where $r := |\boldsymbol{x}-\boldsymbol{y}|$ is a condensed notation for the distance between $\boldsymbol{x}$ and $\boldsymbol{y}$ and $d > 0$ is a preselected cut-off radius. The function b serves to localize the traction density in accordance with condition C1. To this end, a smooth window function based on a b-spline $b : \mathbb{R}_+ \to [0,1]$ is applied:

$$b(r) := \begin{cases} 1 - 3r^2, & r < 1/3, \\ 3/2 - 3r + (3/2)r^2, & 1/3 \leqslant r \leqslant 1, \\ 0, & \text{otherwise}, \end{cases}$$

This is a common kernel in the realm of smooth particle hydrodynamics. The vector-valued function $\boldsymbol{d}$ accounts for the directional dependence in condition C2:

$$\boldsymbol{d}(\boldsymbol{x},\boldsymbol{y}) = r^{-1}(\boldsymbol{x}-\boldsymbol{y}).$$

The function v serves to impose the non-contiguity condition C3 and the reciprocity Principle C5:

$$v(\boldsymbol{x},\boldsymbol{y}) = |r^{-1}(\boldsymbol{x}-\boldsymbol{y})\cdot(\boldsymbol{n}(\boldsymbol{x}) - \boldsymbol{n}(\boldsymbol{y}))|. \tag{35}$$

Finally, the factor r^{-1} serves to introduce the singular behavior of the traction density to fulfill condition C4. Another important argument for selecting the particular form of v in (35) and the r^{-1} dependence, is that these lead to a traction density that can be conveniently expressed in terms of the singular kernel $\partial_{\boldsymbol{n}}G$ according to (6) in the double-layer potential.

The expression for v in (35) warrants some further elaboration. To prove that the corresponding traction density satisfies condition C3, a parametrization $(0,L) \ni s \mapsto \boldsymbol{z}(s) \in \Gamma$ is considered. Note that for $|\alpha| < \delta$ and $\delta \to +0$, it holds that

$$\begin{aligned}\boldsymbol{F}(\boldsymbol{z}(s),\boldsymbol{z}(s+\alpha)) &= b\left(\frac{|\boldsymbol{z}(s)-\boldsymbol{z}(s+\alpha)|}{d}\right)\left|\frac{\boldsymbol{z}(s)-\boldsymbol{z}(s+\alpha)}{|\boldsymbol{z}(s)-\boldsymbol{z}(s+\alpha)|^3}\cdot\left(\frac{\operatorname{rot}D\boldsymbol{z}(s)}{|D\boldsymbol{z}(s)|}-\frac{\operatorname{rot}D\boldsymbol{z}(s+\alpha)}{|D\boldsymbol{z}(s+\alpha)|}\right)\right|(\boldsymbol{z}(s)-\boldsymbol{z}(s+\alpha)) \\ &= b\left(\frac{|D\boldsymbol{z}(s)\,\alpha+o(\delta)|}{d}\right)\left|\frac{-D\boldsymbol{z}(s)\,\alpha+o(\delta)}{|D\boldsymbol{z}(s)\,\alpha+o(\delta)|^3}\cdot\left(\frac{D\boldsymbol{z}(s)\cdot D^2\boldsymbol{z}(s)\operatorname{rot}D\boldsymbol{z}(s)\,\alpha}{|D\boldsymbol{z}(s)|^3}-\frac{\operatorname{rot}D^2\boldsymbol{z}(s)\,\alpha}{|D\boldsymbol{z}(s)|}+o(\delta)\right)\right|(-D\boldsymbol{z}(s)\,\alpha+o(\delta)) \\ &= \boldsymbol{C}_{\boldsymbol{z}}(s)\frac{\alpha}{|\alpha|}+o(1)\end{aligned} \tag{36}$$

where $o(\cdot)$ denotes the Landau symbol with the property that $o(\delta^\beta)/|\delta^\beta| \to 0$ as $\delta \to 0$ for all $\beta \geqslant 0$ and

$$\boldsymbol{C}_{\boldsymbol{z}}(s) = -\left|\frac{D\boldsymbol{z}(s)}{|D\boldsymbol{z}(s)|}\cdot\left(\frac{D\boldsymbol{z}(s)\cdot D^2\boldsymbol{z}(s)\operatorname{rot}D\boldsymbol{z}(s)}{|D\boldsymbol{z}(s)|^3}-\frac{\operatorname{rot}D^2\boldsymbol{z}(s)}{|D\boldsymbol{z}(s)|}\right)\right|D\boldsymbol{z}(s)$$

supposing that all the above derivatives exist. Hence, the leading order term of $\boldsymbol{F}(\boldsymbol{z}(s),\boldsymbol{z}(s+\alpha))$ corresponds to an odd function in α, and its integral on a symmetric interval around $\alpha = 0$ vanishes. More precisely, selecting Γ_δ in (33) according to

$$\Gamma_\delta = \{\boldsymbol{x} \in \Gamma : \boldsymbol{x} = \boldsymbol{z}(s+\alpha), |\alpha| < \delta\} \tag{37}$$

in the limit $\delta \to +0$ it is seen that

$$\begin{aligned}&\frac{1}{\operatorname{meas}\Gamma_\delta}\left|\int_{\Gamma_\delta}\boldsymbol{F}(\boldsymbol{z}(s),\boldsymbol{y})\,d\sigma(\boldsymbol{y})\right| \\ &= \frac{1}{2\delta|D\boldsymbol{z}(s)|+o(\delta)}\left|\int_{-\delta}^{\delta}\left(\boldsymbol{C}_{\boldsymbol{z}}(s)\frac{\alpha}{|\alpha|}+o(1)\right)|D\boldsymbol{z}(s)+o(1)|\,d\alpha\right| = o(1),\end{aligned} \tag{38}$$

and, hence, for each $\varepsilon > 0$ there exists a $\delta > 0$ such that (33) holds with $\boldsymbol{x} = \boldsymbol{z}(s)$.

Summarizing, the contact-induced traction on the structure reads:

$$\begin{aligned}\boldsymbol{\varphi}_{\boldsymbol{z}}(\boldsymbol{x}) &:= \zeta\oint_{\partial\Omega}\boldsymbol{F}(\boldsymbol{x},\boldsymbol{y})\,d\sigma(\boldsymbol{y}) \\ &= 2\zeta\oint_{\partial\Omega}b(\boldsymbol{x},\boldsymbol{y})\left|\frac{(\boldsymbol{x}-\boldsymbol{y})\cdot(\boldsymbol{n}(\boldsymbol{x})-\boldsymbol{n}(\boldsymbol{y}))}{2r^2}\right|\frac{\boldsymbol{x}-\boldsymbol{y}}{r}\,d\sigma(\boldsymbol{y}) \\ &= 2\pi\zeta\oint_{\partial\Omega}b(\boldsymbol{x},\boldsymbol{y})|\partial_{\boldsymbol{n}}G(\boldsymbol{x},\boldsymbol{y})+\partial_{\boldsymbol{n}}G(\boldsymbol{y},\boldsymbol{x})|\frac{\boldsymbol{x}-\boldsymbol{y}}{r}\,d\sigma(\boldsymbol{y}).\end{aligned} \tag{39}$$

In a numerical procedure, the expression $\boldsymbol{\varphi}_{\boldsymbol{z}}(\boldsymbol{x})$ is required at certain integration points, $\{\boldsymbol{x}_i\}$. Moreover, for each $\boldsymbol{x} \in \{\boldsymbol{x}_i\}$, the integral on $\partial\Omega$ in (39) is computed by means of a quadrature rule, which involves determining the value of the integrand at points $\{\boldsymbol{y}_j\}$. Hence, the value of the integrand is required for all pairs of points $(\boldsymbol{x},\boldsymbol{y}) \in \{\boldsymbol{x}_i\}\times\{\boldsymbol{y}_j\}$. The final expression in (39) conveys that $\boldsymbol{\varphi}_{\boldsymbol{z}}$ can indeed be efficiently computed, because the values of the singular kernel $\partial_{\boldsymbol{n}}G(\boldsymbol{x},\boldsymbol{y})$ and of the relative positions $\boldsymbol{x}-\boldsymbol{y}$ at $\{\boldsymbol{x}_i\}\times\{\boldsymbol{y}_j\}$ have already been computed in the numerical approximation of the double-layer potential (4b).

To establish that the contact-induced traction defines a meaningful load on the structure, it must be shown that the map:

$$\boldsymbol{w} \mapsto \int_0^T\int_0^L \boldsymbol{w}(t,s)\cdot\boldsymbol{\varphi}_{\boldsymbol{z}}\circ\boldsymbol{z}(t,s)\,|D\boldsymbol{z}(t,s)|\,ds\,dt \tag{40}$$

defines a continuous linear functional on $L^2(0,T;\boldsymbol{H}_0^2(0,L))$; cf. (15) and (22). First note that by Hölder's inequality,

$$\begin{aligned}&\left|\int_0^T\int_0^L \boldsymbol{w}(t,s)\cdot\boldsymbol{\varphi}_{\boldsymbol{z}}\circ\boldsymbol{z}(t,s)\,|D\boldsymbol{z}(t,s)|\,ds\,dt\right| \\ &\quad\leqslant \|\boldsymbol{w}\|_{L^2(0,T;\boldsymbol{L}^\infty(0,L))}\|D\boldsymbol{z}\|_{L^\infty(0,T;\boldsymbol{L}^\infty(0,L))}\|\boldsymbol{\varphi}_{\boldsymbol{z}}\circ\boldsymbol{z}\|_{L^2(0,T;\boldsymbol{L}^1(0,L))}\end{aligned} \tag{41}$$

Hence, by the same arguments as in Section 2.3, it remains to bound the right-most factor in (41). The function $\boldsymbol{\varphi}_{\boldsymbol{z}} \circ \boldsymbol{z}(t,s)$ can be expanded into:

$$\begin{aligned}\boldsymbol{\varphi}_{\boldsymbol{z}} \circ \boldsymbol{z}(t,s) &= \zeta \oint_{\partial\Omega} \boldsymbol{F}(\boldsymbol{z}(t,s),\boldsymbol{y})\, d\sigma_t(\boldsymbol{y}) \\ &= 2\pi\zeta \oint_{\partial\Omega} \left(-\partial_{\boldsymbol{n}} G(\boldsymbol{z}(t,s),\boldsymbol{y}) - \partial_{\boldsymbol{n}} G(\boldsymbol{y},\boldsymbol{z}(t,s))\right)\boldsymbol{\Theta}(\boldsymbol{z}(t,s),\boldsymbol{y})\, d\sigma_t(\boldsymbol{y})\end{aligned} \tag{42}$$

where

$$\boldsymbol{\Theta}(\boldsymbol{x},\boldsymbol{y}) = b\left(\frac{|\boldsymbol{x}-\boldsymbol{y}|}{d}\right) \mathbb{1}_{\mathrm{supp}(v)}(\boldsymbol{x},\boldsymbol{y}) \frac{\boldsymbol{x}-\boldsymbol{y}}{|\boldsymbol{x}-\boldsymbol{y}|} \tag{43}$$

with $\mathbb{1}_{\mathrm{supp}(v)}$ the characteristic function of the support of v according to (35), i.e., $\mathbb{1}_{\mathrm{supp}(v)}(\boldsymbol{x},\boldsymbol{y})$ is 1 if $v(\boldsymbol{x},\boldsymbol{y}) \neq 0$ and 0 otherwise. Because $\boldsymbol{\Theta}$ in the ultimate expression depends on $\boldsymbol{z}$, standard results on continuity of the double-layer potential and its adjoint do not suffice to bound the right-most factor in (41). A detailed analysis of $\boldsymbol{\varphi}_{\boldsymbol{z}} \circ \boldsymbol{z}(t,s)$ is technical and is beyond the scope of this paper, and boundedness of $\|\boldsymbol{\varphi}_{\boldsymbol{z}} \circ \boldsymbol{z}\|_{L^2(0,T;\boldsymbol{L}^1(0,L))}$ is left as a conjecture. However, in support of this conjecture, note that the asymptotic result in (36) implies that, under suitable smoothness conditions on $\boldsymbol{z}$, the traction density $\boldsymbol{F}(\boldsymbol{z}(s),\boldsymbol{z}(s+\alpha))$ is bounded at the singularity of $\partial_{\boldsymbol{n}} G$, i.e., in the limit as $\alpha \to 0$.

3. Numerical approximation and solution

In this section, the numerical approximation of the aggregated fluid–structure-interaction problem are considered, composed of the weak form of the boundary-integral formulation of the fluid equations (7), the weak formulation of the membrane equations and the compatibility condition (26), and the kinematic and dynamic transmission conditions (19) and (20). Section 3.1 presents the spatial and temporal discretizations of the fluid and structure subproblems. The aggregated system is solved by means of a partitioned iterative solution procedure, which is elaborated in Section 3.2.

3.1. Finite-element approximations

Recalling that the initial wet boundary Γ_0 and the inflow boundary Γ_{in} of the fluid domain are parametrized with respect to the arc-length intervals $(0,L)$ and (L,Λ), a sequence of nested regular partitions $\mathcal{S}^h$ of these intervals is introduced, parametrized by a strictly decreasing sequence of mesh parameters $h \in \{h_0, h_1, \ldots\}$. For each h, the partition $\mathcal{S}^h$ provides a cover of $(0,L)$ and (L,Λ) by disjoint open subsets $\{\kappa_1^h, \kappa_2^h, \ldots\}$. The quasi-uniformity of the partitions implies that there exist moderate, positive constants $\underline{c}$ and $\bar{c}$, independent of h, such that for each $\kappa \in \mathcal{S}^h$ it holds that $\underline{c}h \leqslant \mathrm{meas}\,\kappa \leqslant \bar{c}h$. The nesting of the partitions implies that whenever $h_1 < h_0$, for each subset $\kappa \in \mathcal{S}^{h_1}$ there exists a subset $\varkappa \in \mathcal{S}^{h_0}$ such that $\kappa \subseteq \varkappa$. A partition $\mathcal{S}^h$ and the subintervals it contains are referred to as a *mesh* and *elements*, respectively.

The partitions form the substructure of the finite-element approximation spaces for the fluid and structure subproblems,

$$\mathbb{S}^h := \left\{\boldsymbol{M} \in \boldsymbol{C}^1(0,L) : \boldsymbol{M}|_\kappa \in \mathbb{P}^3(\kappa,\mathbb{R}^2)\ \forall \kappa \in \mathcal{S}^h,\ \kappa \subset (0,L)\right\}, \tag{44a}$$

$$\mathbb{F}_{\mathrm{p}}^h := \left\{N \in C^0(0,\Lambda) : N|_\kappa \in \mathbb{P}^1(\kappa,\mathbb{R})\ \forall \kappa \in \mathcal{S}^h;\ N(0) = N(\Lambda)\right\}, \tag{44b}$$

respectively, where $\mathbb{P}^p(\kappa,\mathbb{R}^n)$ represents the class of polynomials of degree $\leqslant p$ from κ into $\mathbb{R}^n$. The approximation space $\mathbb{S}^h \subset \boldsymbol{H}^2(0,L)$ (resp. $\mathbb{F}_{\mathrm{p}}^h \subset H_{\mathrm{p}}^1(0,\Lambda)$, viz., the periodic functions in $H^1(0,\Lambda)$) is $\boldsymbol{H}^2(0,L)$-conforming (resp. $H_{\mathrm{p}}^1(0,\Lambda)$ conforming). On account of the regularity and nesting properties of the meshes, the sequence of approximation spaces $\mathbb{S}^h$ has the approximability property [14]. This means that $\mathbb{S}^h$ is nested and asymptotically dense in $\boldsymbol{H}^2(0,L)$, i.e., $\mathbb{S}^{h_0} \subset \mathbb{S}^{h_1} \subset \cdots \subseteq H^2(0,L)$ and $\mathrm{dist}(\mathbb{S}^h, \boldsymbol{H}^2(0,L)) \to 0$ as $h \to 0$. Similarly, $\mathbb{F}_{\mathrm{p}}^h$ is a sequence of asymptotically dense, nested subspaces in $H_{\mathrm{p}}^1(0,\Lambda)$. The basis functions (coinciding with test functions) for the spaces $\mathbb{S}^h$ and $\mathbb{F}_{\mathrm{p}}^h$ are furnished by the Hermite and linear functions (cf. [14]) respectively, as illustrated in Fig. 2.

To facilitate the evaluation of the singular integrals in the boundary-element formulation of the fluid, the element-wise polynomial representation of the boundary provided by the approximation of the structure position is not used. Instead, a continuous element-wise linear approximation of the domain boundary is selected, which nodally coincides with the structure position or, along the section associated with the inflow boundary, with the initial configuration. This is illustrated in Fig. 2. In particular, for an approximate structural position $\boldsymbol{z}^h \in \mathcal{S}^h$, the boundary of the approximate fluid domain is parametrized according to $\partial\Omega^h = \{\boldsymbol{x} \in \mathbb{R}^2 : \boldsymbol{x} = \tilde{\boldsymbol{z}}^h(s), s \in (0,\Lambda)\}$, where $\tilde{\boldsymbol{z}}^h$ is the unique function defined by:

$$\begin{aligned}&\{\tilde{\boldsymbol{z}}^h \in \boldsymbol{C}^0(0,\Lambda) : \tilde{\boldsymbol{z}}^h|_\kappa \in \mathbb{P}^1(\kappa,\mathbb{R}^2)\ \forall \kappa \in \mathcal{S}^h; \\ &\tilde{\boldsymbol{z}}^h|_{\mathcal{N}^h\cap[0,L)} = \boldsymbol{z}^h|_{\mathcal{N}^h\cap[0,L)};\ \tilde{\boldsymbol{z}}^h|_{\mathcal{N}^h\cap[L,\Lambda]} = \boldsymbol{\chi}_0|_{\mathcal{N}^h\cap[L,\Lambda]}\},\end{aligned} \tag{45}$$

where $\mathcal{N}^h := \cup_{\kappa\in\mathcal{S}^h} \partial\kappa$ is the set of nodes corresponding to $\mathcal{S}^h$. Singular contributions to the integrals in (7) occur on elements where both ψ and ϕ are supported. Denote the linear basis on $\tilde{\boldsymbol{z}}^h(\kappa)$ by $N_i^\kappa, i \in \{0,1\}$. For convenience of notation $J_\kappa := |D\tilde{\boldsymbol{z}}^h|_\kappa \mathrm{meas}\,\kappa$ is introduced, which is a constant on κ by virtue of the approximation $\tilde{\boldsymbol{z}}^h$ of the configuration. The singular contributions can than be computed by combinations of the integrals

$$\begin{aligned}(N_i, KN_j)_{L^2(\tilde{\boldsymbol{z}}^h(\kappa))} &= 0, \\ (N_i, VN_j)_{L^2(\tilde{\boldsymbol{z}}^h(\kappa))} &= (6 + (-1)^{i+j} - 4\log J_\kappa)\frac{J_\kappa^2}{2\pi}.\end{aligned}$$

The contributions of element pairs, including neighboring elements, are computed using standard high-order Gaussian quadrature rules. The convergence tests in Section 4 indicate that this basic approach is sufficient. However, an essential improvement in efficiency can be attained by means of, for instance, adaptive quadrature schemes.

For the temporal discretization of the structure equation (26), an implicit backward-Euler approximation is used. To facilitate the formulation of the discretization of the fluid–structure-interaction problem, denote by $\boldsymbol{z}_0^h \in \mathbb{S}^h$ a suitable approximation to the initial position $\boldsymbol{\chi}_0$ such that $\boldsymbol{z}_0^h|_{\{0,L\}} = \boldsymbol{\chi}_0|_{\{0,L\}}$, and by $\mathbb{S}_0^h = \{\boldsymbol{z}^h \in \mathbb{S}^h : \boldsymbol{z}|_{\{0,L\}} = 0\}$ the functions in $\mathbb{S}^h$ that vanish at the end points of the interval $(0,L)$. Denoting by $n \in \mathbb{N}$ the time step and by τ the time step size (such that $\boldsymbol{z}_n^h = \boldsymbol{z}^h(t_n)$ with $t_n = n\tau$), the discrete approximation of the aggregated fluid–structure-interaction problem can then be formulated as:

For $n = 1,2,\ldots$, find $\left(\boldsymbol{z}_n^h, \lambda_n, \phi_n^h, \zeta_n\right) \in (\boldsymbol{z}_0^h + \mathbb{S}_0^h) \times \mathbb{R} \times \mathbb{F}_{\mathrm{p}}^h \times \mathbb{R}$, such that for all $(\boldsymbol{w},\mu,\psi,\upsilon) \in \mathbb{S}_0^h \times \mathbb{R} \times \mathbb{F}_{\mathrm{p}}^h \times \mathbb{R}$, there holds:

$$\begin{aligned}&\tau^{-2}(\boldsymbol{z}_n^h, \boldsymbol{w})_{\boldsymbol{L}^2(0,L)} + a_{\mathrm{s}}(\boldsymbol{z}_n^h; \boldsymbol{w}) - \lambda_n(\mathrm{rot}\, D\boldsymbol{z}_n^h, \boldsymbol{w})_{\boldsymbol{L}^2(0,L)} \\ &+ \frac{\vartheta}{2}(|\nabla_\Gamma \phi_n^h|^2 \circ \tilde{\boldsymbol{z}}_n^h\, \mathrm{rot}\, D\boldsymbol{z}_n^h, \boldsymbol{w})_{\boldsymbol{L}^2(0,L)} \\ &+ \frac{\vartheta}{2}((\tau^{-1}(\boldsymbol{z}_n^h - \boldsymbol{z}_{n-1}^h)\cdot(|D\boldsymbol{z}_n^h|^{-1}\,\mathrm{rot}\, D\boldsymbol{z}_n^h))^2\,\mathrm{rot}\, D\boldsymbol{z}_n^h, \boldsymbol{w})_{\boldsymbol{L}^2(0,L)} \\ &- (|D\boldsymbol{z}_n^h|\boldsymbol{F}_{\boldsymbol{z}_n^h} \circ \boldsymbol{z}_n^h, \boldsymbol{w})_{\boldsymbol{L}^2(0,L)} + \mu Q(\boldsymbol{z}_n^h) + \left(\frac{1}{2}\phi_n^h + K\phi_n^h, \psi\right)_{L^2(\partial\Omega_n^h)} \\ &- (V(|D\tilde{\boldsymbol{z}}_n^h|^{-1}\,\mathrm{rot}\, D\tilde{\boldsymbol{z}}_n^h \cdot (\tau^{-1}(\tilde{\boldsymbol{z}}_n^h - \tilde{\boldsymbol{z}}_{n-1}^h)) \circ (\tilde{\boldsymbol{z}}_n^h)^{-1}, \psi)_{L^2(\Gamma_n^h)} \\ &+ \upsilon(\phi_n^h, 1)_{L^2(\partial\Omega_n^h)} + \zeta_n(\psi, 1)_{L^2(\partial\Omega_n^h)} = \tau^{-2}(\boldsymbol{z}_{n-1}^h, \boldsymbol{w})_{\boldsymbol{L}^2(0,L)} \\ &+ \tau^{-1}(\boldsymbol{v}_{n-1}^h, \boldsymbol{w})_{\boldsymbol{L}^2(0,L)} + \mu c(t_n) + (Vq, \psi)_{L^2(\Gamma_{\mathrm{in}}^h)}.\end{aligned} \tag{46}$$

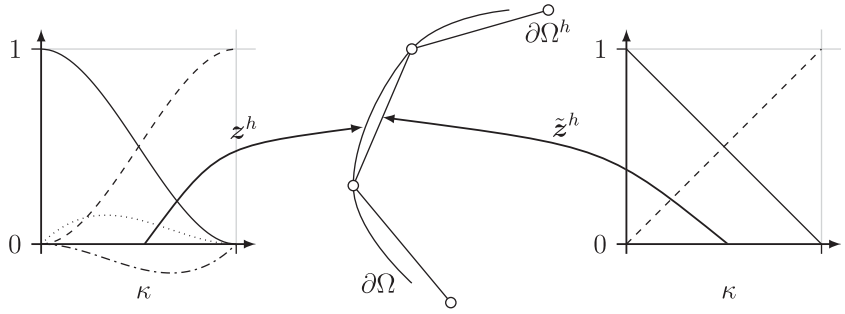

Fig. 2. Schematic of basis functions of the approximation spaces in the parametric domain. On the left, the Hermite basis of $\mathbb{S}^h$ is depicted; and on the right, the linear basis of $\mathbb{F}^h_{\mathrm{p}}$. In the center, the isoparametric representation of the fluid and structure in the current domain at their mutual interface is shown, where $\circ$ indicates the collocated nodes.

Furthermore, $\boldsymbol{v}_0^h$ denotes a suitable approximation of the initial velocity and $\boldsymbol{v}_n^h = \tau^{-1}(\boldsymbol{z}_n^h - \boldsymbol{z}_{n-1}^h)$ for $n = 1, 2, \ldots$; cf. (26) and (7). It is to be noted that the term pertaining to the pressure level p_0 in (26) has been merged with the Lagrange-multiplier term, in accordance with the exposition in Section 2.4. Moreover, in (46), the $|\nabla\phi|^2$ term in (26) has been expanded in accordance with the ultimate identity in (20), and the orthogonality conditions $(\phi, 1)_{L^2(\partial\Omega_t)} = 0$ and $(\psi, 1)_{L^2(\partial\Omega_t)} = 0$ in (7) are instead imposed by means of Lagrange multipliers.

3.2. Partitioned solution of coupled system

Having fixed solution methods for both the fluid and structure subsystems, the partitioned solution of the coupled system is elaborated upon in this section, see Table 1. A linear extrapolation of the initial data serves as a first approximation of the new coupled solution. Within a fluid–structure subcycle, a structural solve is performed first, to ensure compatibility of the fluid boundary data. The subcycle is considered converged if the norm of the structure residual is below the tolerance before a Newton solve is performed. In performing Newton iterations, the pressure and contact loads are treated explicitly whereas the stiffness semilinear form and volume constraint are consistently linearized as

$$\langle \delta a_{\mathrm{s}}(\boldsymbol{z}_n^h; \boldsymbol{w}), \delta\boldsymbol{z}\rangle = ([(1 - |D\boldsymbol{z}_n^h|^{-1})\mathrm{Id} + |D\boldsymbol{z}_n^h|^{-3} D\boldsymbol{z}_n^h \otimes \boldsymbol{z}_n^h] D\delta\boldsymbol{z}, D\boldsymbol{w})_{\boldsymbol{L}^2(0,L)} + \epsilon(\delta\boldsymbol{z}, \boldsymbol{w})_{\boldsymbol{H}^2_{\mathrm{sem}}(0,L)}$$

and

$$\langle \delta\langle \delta Q(\boldsymbol{z}_n^h), \boldsymbol{w}\rangle, \delta\boldsymbol{z}\rangle = (\mathrm{rot}\, D\delta\boldsymbol{z}, \boldsymbol{w})_{\boldsymbol{L}^2(0,L)}$$

respectively.

The return statement is not reached if either the coupling iteration or the structure solve does not converge due to, for instance, large contact forces. This high temporary stiffness of the problem is resolved by invoking the simplest possible time adaptivity, where the time step is resolved with increasingly finer time steps $2^{-k}\tau$ until the iterations converge. At the subsequent time level, k is coarsened according to $k = \max(k-1, 0)$.

Though performing a linearization on the aggregate fluid–structure system is known to improve convergence of the discrete coupled problem, the complexity rises considerably. The $\boldsymbol{z}_n^h$-derivative of the fluid subproblem is highly nontrivial due to the $\boldsymbol{z}_n^h$-dependence of the kernels. For this reason, a partitioned solution strategy was preferred above a monolithic scheme.

4. Numerical examples

To demonstrate the performance of the finite-element/boundary-element (FE/BE) approach proposed here, first a convergence study is performed on the case of a pancake-shaped domain, adapted from [29,6], see Section 4.1. Secondly, a simple folded configuration is considered, to observe the response and convergence rates in the presence of contact forces. Note that the derivation of convergence rates for coupled problems is very technical, see for instance [16]. The exposition below is restricted to the experimentally observed convergence rates.

Table 1
Partitioned solution algorithm in Python™ pseudo code, given numerical parameters $(\tau, \texttt{imax}, \texttt{jmax}, \texttt{TOL})$, and input $(\texttt{z}(t,\cdot), \texttt{z}(t-\tau,\cdot), \phi_t, q, c_t)$. For simplicity, the Lagrange multipliers have been incorporated into the respective solution vectors. Note that indices do not denote tensor entries, but iterates.

```
z_00, φ_0 = extrapolate(τ, z(t,·), z(t−τ,·), φ_t)

# Coupling iteration
for 0 ⩽ i < imax:

  # Structure solve
  for 0 ⩽ j < jmax:
    r_ij = assembleResidual(z_ij, z(t,·), φ_i, c_t, q, τ)
    if ‖r_ij‖_{L²} < TOL: break
    (δr)_ij = assembleTangent(z_ij)
    z_{ij+1} -= [δr]_ij^{-1} r_ij

  # Return statement
  if not j: return z_ij

  # Fluid solve
  Vh_i, K_i = assembleFluid(z_ij, z(t,·))
  φ_{i+1} = [1/2 + K]_i^{-1} Vh_i
```

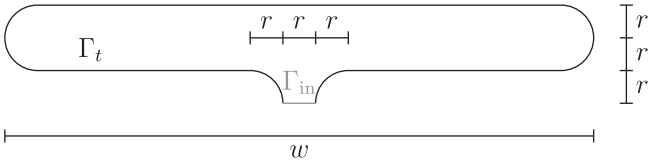

Fig. 3. Pancake-shaped domain, initial geometry.

4.1. Pancake-shaped domain

The initial configuration, $\boldsymbol{\chi}_0$, is as given in Fig. 3 with geometrical parameters $r = 1/3$, $w = 4$. Furthermore the mass ratio ϑ is set to 0.1, and perform spatial and temporal convergence tests with regularization set to $\epsilon = 1 \times 10^{-4}$. The parametric domain is divided into elements of size $h \in L/\{24, 48, 72, 96, 144, 288\}$. The time domain $(0, T)$ is divided into increments of $\tau \in \mathrm{per}/2^{\{5,\ldots,10\}}$ with $\mathrm{per} = (\Lambda/\pi)^2$ an approximation of the period of the first eigenmotion (based on the flexural term). Finally, the inflow is specified as $q = \overline{q}\sigma(s - L)\theta(t)$, with

$$\sigma(s) = 4s(r - s)/r^2,$$

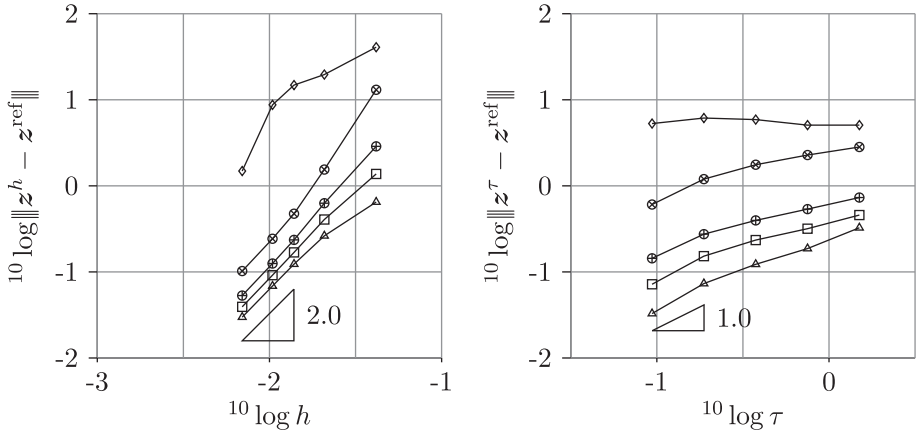

Fig. 4. Convergence behavior in the space–time norm with symbols $\{\triangle,\square,\oplus,\otimes,\diamond\}$ representing time levels $t=\{0.750,3.00,12.0,192,400\}$, respectively.

$$\theta(t)=\frac{1}{t_2}\begin{cases}(1-\cos(\pi t/t_1))/2, & 0<t\leqslant t_1,\\ 1, & t_1<t\leqslant t_2,\\ (1+\cos(\pi(t-t_2)/t_1))/2, & t_2<t\leqslant t_1+t_2,\\ 0, & t_1+t_2<t.\end{cases}$$

In these relations $t_1=100$, $t_2=2t_1$, $T=4t_1$ and the mean influx $\bar{q}=(|\Omega(0)|-|\Omega_t|)/t_2$. The initial volume can be found in terms of w and r[1] and the final volume is specified as $|\Omega_t|=1.05\Lambda^2/4\pi$. Note that the mean flux has a negative sign as it is directed into the enclosure.

The convergence behavior is assessed in the space–time norm of the structure defined by

$$|||\,\boldsymbol{z}\,|||:=\|\boldsymbol{z}\|_{L^2(0,T;\boldsymbol{H}^2(0,L))}=\left(\int_0^T\int_0^L\sum_{\alpha\leqslant 2}|D^\alpha\boldsymbol{z}|^2\,ds\,dt\right)^{1/2}\tag{47}$$

and is plotted in Fig. 4, with reference solution $\boldsymbol{z}^{\mathrm{ref}}$ obtained from the finest discretization in space and time. Spatial convergence is given in the left panel. The optimal (quadratic) convergence rate of the decoupled structural problem seems to be preserved in the initial response. This trend breaks down when simulation times increase and phase-lag dominates the errors. This is due to the fact that, on long time intervals, marginal phase differences cause large deviations in the norm. Snapshots of the associated response are given at different time-levels in Fig. 5.

For temporal convergence (right panel) the linear rate expected of the backward Euler scheme is retained. Also, a linear increase in time of the error norm is observed initially, just like in the spatial convergence case. A reduction in the convergence rate is observed as the time interval increases because the phase-lag precludes correlation between the different time-steps. It is however anticipated that even for long time intervals, the asymptotic first-order convergence is recovered at very small time steps.

In the above pancake case, a second order h-convergence rate of the coupled response $\boldsymbol{z}$ in the $W(0,T)$ space–time norm is observed. Surprisingly, this is not hampered by the convergence of the fluid load (see Eq. (22))

$$\boldsymbol{w}\mapsto\int_0^T\int_0^L\boldsymbol{w}(t,s)\cdot(p\circ\boldsymbol{z}(t,s)\,\mathrm{rot}\,D\boldsymbol{z}(t,s))\,ds\,dt.$$

which is expected to exhibit $O(h)$ convergence, as p depends on the Γ-gradient of $\phi\in\mathbb{F}^h$, the space of piece-wise linears. It is conjectured that the higher-order rate of convergence is caused by the symmetry of the configuration. To verify this conjecture, the following case is considered. A hierarchy of nested meshes and corresponding linear spaces is generated on each level. The pancake geometry of Fig. 3 and fabricated boundary conditions are projected onto the coarsest mesh. In this case the boundary conditions are $g=\boldsymbol{z}'\cdot\boldsymbol{n}$ with

$$\boldsymbol{z}'=\{0.3(|x_1|-r/2),0\},\tag{48}$$

thus, g both satisfies the compatibility constraint (23) and respects the structural boundary conditions. These projections form the input of the fluid problems that are solved at each mesh level. This ultimately yields the desired family of load functionals that can be tested against the projection of

$$\boldsymbol{w}=\{0,\sin(k\pi s/L)\},$$

onto a Hermite space on the finest mesh. Note that the test function is thus identical at each resolution of the convergence analysis, eliminating the effect of this projection on observed convergence rates. The cases $k=1$ and 2 correspond to symmetric and asymmetric test functions $\boldsymbol{w}$, respectively.

Employing a hierarchy of equidistant meshes with $16\cdot\{2,\ldots,15,60\}$ elements, and comparing the errors with respect to the finest approximation, the convergence behavior in Fig. 6 is obtained. Note that the three curves corroborate the above assertions, namely, that the pressure converges with rate 1 in the $\boldsymbol{L}^2(0,L)$ norm, but that the rate for the load functional is 2 in the case of a symmetric $\boldsymbol{w}$. This enables the structure solution to converge with rate 2 as observed in the symmetric pancake case of Section 4.1. In the case of an asymmetric $\boldsymbol{w}$ the convergence rate clearly does not attain this optimal value of 2, although it is steeper than 1.

4.2. Folded configuration

Next, a folded configuration (see Fig. 7) including contact forces is considered. Parameters are set to $\zeta=1.0$, $d=2.0$. The contact force parameters have been chosen to ensure no self-contact occurs throughout the simulations. Fig. 8 illustrates that the membrane exhibits significant wrinkling. These wrinkles are caused by the contact force. The contact force plays a dominant role in the structural response, on account of the so-called *Venturi effect*. This Venturi effect pertains to the phenomenon that the pressure decreases in narrow sections of the fluid domain with nonzero flow. This effect is to be compared to the pressure drop in a converging–diverging channel. The pressure drop causes the membrane on the two opposite sides of the converging section to approach, which in turn causes a local narrowing of the fluid domain, and a corresponding strengthening of the pressure drop. In

[1] It holds that $|\Omega(0)|=2wr-r^2+\pi r^2/2$.

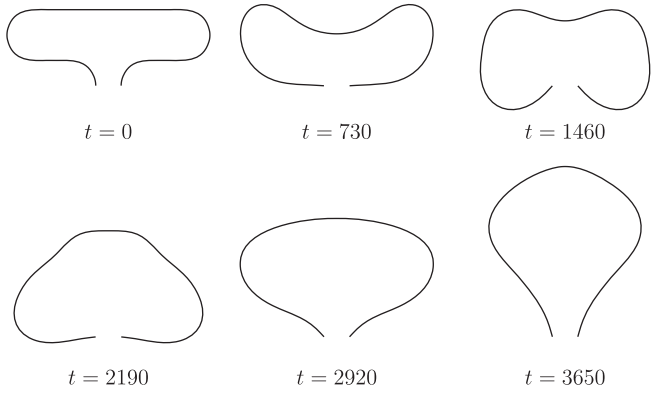

Fig. 5. Snapshots of the pancake response, for $w = 4$, colors indicate the static pressure.

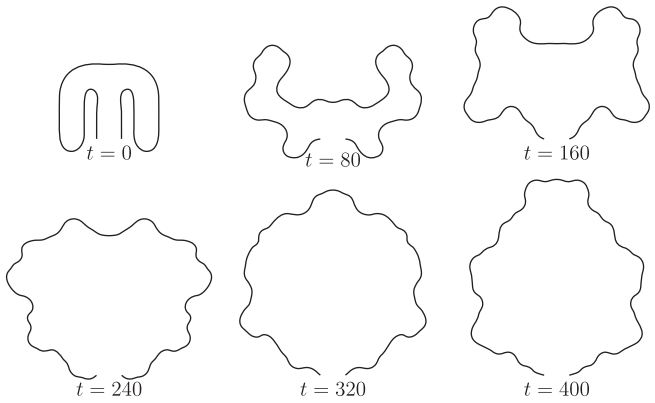

Fig. 8. Snapshots of the response for the folded domain.

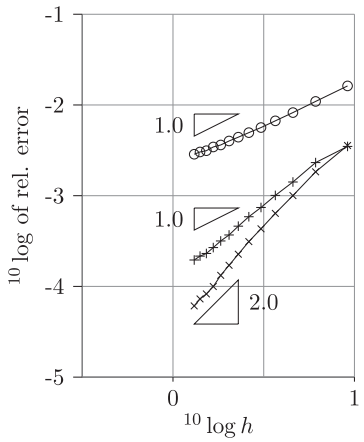

Fig. 6. Convergence of the pressure in the $\boldsymbol{L}^2(0,L)$ norm ($\circ$), and corresponding loads tested against symmetric ($\times$) and asymmetric ($+$) functions.

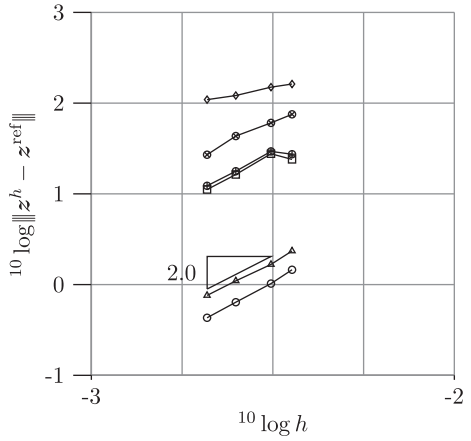

Fig. 9. Convergence behavior for the folded configuration in the space–time norm $|||\cdot|||$ with symbols $\{\circ, \triangle, \square, \oplus, \otimes, \diamond\}$ representing time levels $t \in \{0.26, 1.06, 4.24, 16.95, 67.80, 135.59\}$, respectively.

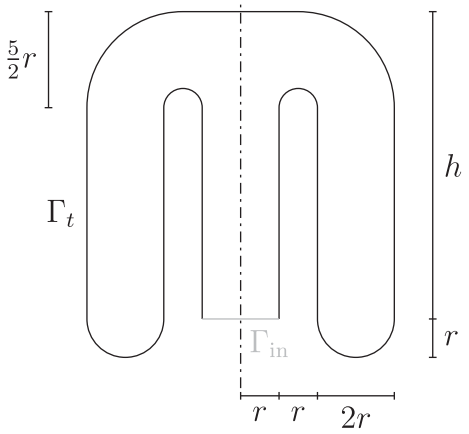

Fig. 7. Initial configuration of folded domain test case.

the absence of contact forces, this process would ultimately lead to a local collapse of the membrane. The aforementioned Venturi effect in fact results in a singular attractive force between sections of the membrane. This singular attractive force must be counteracted by a sufficiently strong singular contact force to avoid collapse of the structure. It is to be noted that the Venturi effect is particular for the considered potential-flow model and that, in contrast, Stokes flow displays a repulsive lubrication effect [37].

Fig. 9 displays the error in the displacement for time step $6.621 \cdot 10^{-2}$ and mesh widths h in $L/\{160, 280, 320, 400, 480, 640\}$ with the last of these the resolution for the reference solution. A fine h is observed to be necessary to be in the asymptotic convergence regime. The error convergence as $h \to 0$ is shown in Fig. 9. It is observed that optimal convergence rates in the norm $|||\cdot|||$ are also recovered in the case of contact forces.

Finally, the computation times are investigated.[2] It is immediately noted, however, that the numbers given are only indicative, as the program has not been optimized. The computations break down as shown in Table 2. Cases I and II correspond to §4.1. The assembly of the full boundary element method (BEM) matrix dominates the simulation time. For these relatively small problems, the solution of linear systems are cheap. Also, the relative contribution of overhead decreases with problem size. For case III we see similar trends as in the first two cases, except a considerably contribution of the contact force assembly, it is more expensive than the remainder of the structure assembly. This is because the non-optimized computation of the contact forces is based on data from the fluid at the quadrature point level, which,

[2] Experiments were conducted on an Intel® Xeon® 2.00 GHz processor.

Table 2
Component-wise computation times as a fraction of the total time. Cases I and II represent the pancake test-case at the coarsest (24 elements) and finest (288 elements) resolution respectively. Case III corresponds to the folded domain case with the repulsive contact potential on the coarsest (160 elements) resolution.

	I	II	III
Structure assembly	0.156	0.322	0.101
Structure solve	0.003	0.016	0.002
Fluid assembly	0.745	0.634	0.694
Fluid solve	0.000	0.000	0.000
Contact force assembly	–	–	0.147
Miscellaneous	0.095	0.027	0.056
Elapsed (h:mm)	0:07	8:01	4:31

at the high quadrature orders used here, incur significant burden in the element integration.

5. Conclusions

A model was presented for the interaction of a membrane with an enclosed fluid described by potential flow. The linearity of the fluid response allows discretization with the boundary element method (BEM). Despite its simplicity, the model poses some theoretical and numerical challenges. Uniqueness results are not available and are not easily acquired. A regularization of the membrane equation is needed for stability. In this work flexural rigidity is introduced for that purpose. As the fluid is enclosed and incompressible, the volume needs to be constrained explicitly. A physical interpretation was derived for the Lagrange multiplier enforcing this constraint, the total internal excess pressure p_0.

The numerical tests show the capabilities of the presented finite-element/boundary-element (FE/BE) coupling scheme. The discretization of the fluid with the boundary element method (BEM), allows for very large deformations without evolving or recreating volumetric meshes. In this sense, it extends the type of problems that can be treated using an ALE-approach.

To counteract self-crossing of the membrane, ubiquitous in the simulation folded inflatable structures, an efficient contact force is introduced. The potential contact force is passive and its computation is feasible because of reuse of components generated in the boundary element method (BEM) formulation of the fluid. An inherent feature of potential flow is the Venturi effect, where pressure forces cause a narrow section in the flow field to contract further. Contraction would lead to collapse and self crossing, which has to be prevented by the contact force. Numerical experiments for a folded configuration revealed that owing to the Venturi effect, the contact forces play a dominant role in the structural response.

Acknowledgements

The authors thank Kris van der Zee of Eindhoven University of Technology for fruitful discussions on the interpretation of the Lagrange multiplier; and Matthias Taus of the Institute for Computational Engineering and Sciences for discussions on the refined regularity of solutions of the boundary integral equation. This research is supported by the Dutch Technology Foundation STW, which is part of the Netherlands Organization for Scientific Research (NWO) and partly funded by the Ministry of Economic Affairs, Agriculture and Innovation (Project Number 10476).

Appendix A. Nondimensionalization

The membrane motion is given as $s,t \mapsto \boldsymbol{z} : [0,L]\times[0,T] \to \mathbb{R}^2$ and governed by

$$\varrho_0 h\boldsymbol{z}'' = EhD(D\boldsymbol{z}(1-|D\boldsymbol{z}|^{-1})) + \left(p_0 - \frac{1}{2}\rho|\nabla\phi|^2\right)\mathrm{rot}\, D\boldsymbol{z}, \tag{A.1}$$

with appropriate initial- and boundary conditions. In this equation ϱ_0, h and E are the membrane density, thickness and stiffness, resp. Furthermore, ρ and ϕ the are the fluid density and potential, resp. For nondimensionalization, two characteristic quantities of the problem are chosen, namely the wave propagation speed in the membrane $c_0 = (E/\varrho_0)^{1/2}$; and a length ℓ, then

$$\boldsymbol{z} = \ell\{\boldsymbol{z}\}, \quad \phi = \ell c_0\{\phi\}, \quad (\cdot)' = c_0\ell^{-1}\{(\cdot)'\}, \quad D = \ell^{-1}\{D\},$$
$$\nabla = \ell^{-1}\{\nabla\}.$$

In the following, the nondimensionalization braces $\{\cdot\}$ have immediately been dropped. Substitution yields a one-parameter wave equation

$$\boldsymbol{z}'' - D(D\boldsymbol{z}(1-|D\boldsymbol{z}|^{-1})) - \left(p_0 - \frac{1}{2}\vartheta|\nabla\phi|^2\right)\mathrm{rot}\, D\boldsymbol{z} = 0, \tag{A.2}$$

with $\vartheta := \rho\ell/\varrho_0 h$ the mass ratio. The dimensionless total pressure $\{p_0\} = p_0\ell/(\varrho_0 c_0^2 h) = p_0\ell/Eh$. Thus, effectively, time derivatives have been scaled by c_0 w.r.t. spatial derivatives, i.e., choosing $\ell = 1$ yields $h/1 = \{h\}$ and $\tau\cdot c_0/1 = \{\tau\}$. Secondly, the influence of stiffness is through (i) this scaling of derivatives; and (ii) the total pressure.

For the fluid, the original relation is retrieved,

$$\begin{aligned}\frac{1}{2}\phi(\boldsymbol{x}) + \frac{1}{2\pi}\oint_{\partial\Omega}\frac{(\boldsymbol{x}-\boldsymbol{y})\cdot\boldsymbol{n}(\boldsymbol{y})}{|\boldsymbol{x}-\boldsymbol{y}|^2}\phi(\boldsymbol{y})d\sigma(\boldsymbol{y}) &= -\frac{1}{2\pi}\oint_{\partial\Omega}(\log\ell + \log|\boldsymbol{x}-\boldsymbol{y}|)h(\boldsymbol{y})d\sigma(\boldsymbol{y}) \\ &= -\frac{1}{2\pi}\oint_{\partial\Omega}(\log|\boldsymbol{x}-\boldsymbol{y}|)h(\boldsymbol{y})d\sigma(\boldsymbol{y}),\end{aligned} \tag{A.3}$$

where the last equality follows from the compatibility condition on h.

References

[1] S. Antman, The equations for large vibrations of strings, Am. Math. Mon. 87 (1980) 359–370.
[2] S. Antman, Nonlinear problems of elasticity, in: Applied Mathematical Sciences, Springer, Verlag, New York, 1995.
[3] S. Brenner, L. Scott, The Mathematical Theory of Finite Element Methods, Texts in Applied Mathematics, second ed., vol. 15, Springer, Berlin, 2002.
[4] D. Brunner, M. Junge, L. Gaul, A comparison of FE–BE coupling schemes for large-scale problems with fluid-structure interaction, Int. J. Numer. Methods Eng. 77 (2009) 664.
[5] C. Carstensen, E. Stephan, Adaptive coupling of boundary elements and finite elements, Math. Modell. Numer. Anal. 29 (1995) 779–817.
[6] F. Cirak, R. Radovitzky, A Lagrangian–Eulerian shell–fluid coupling algorithm based on level sets, Comput. Struct. 83 (2005) 491–498.
[7] M. Costabel, Boundary integral operators on Lipschitz domains: elementary results, SIAM J. Math. Anal. 19 (1988) 613–626.
[8] M. Costabel, Time-dependent problems with the boundary integral equation method, in: E. Stein, R. Borst, T. Hughes (Eds.), Encyclopedia of Computational Mechanics, Fundamentals, vol. 2, John Wiley & Sons, Ltd., 2004, pp. 703–721 (Chapter 25).
[9] O. Czygan, O. von Estorff, Fluid-structure interaction by coupling BEM and nonlinear FEM, Eng. Anal. Boundary Elem. 26 (2002) 773–779.
[10] R. Dautray, J.-L. Lions, Mathematical Analysis and Numerical Methods for Science and Technology, Evolution Problems II, vol. 6, Springer, New York, 1984.
[11] C. Domínguez, E. Stephan, M. Maischak, A FE–BE coupling for a fluid–structure interaction problem: hierarchical a posteriori error estimates, Numer. Methods Partial Differ. Equ. 28 (2011) 1417–1439.
[12] W. E, Principles of Multiscale Modelling, Cambridge University Press, 2011.
[13] W. Elleithy, R. Grzhibovskis, An adaptive domain decomposition coupled finite element–boundary element method for solving problems in elasto-plasticity, Int. J. Numer. Methods Eng. 79 (2009) 1019–1040.
[14] A. Ern, J.L. Guermond, Theory and practice of finite elements, in: S. Antman, J. Marsden, L. Sirovich (Eds.), Applied Mathematical Science, vol. 159, Springer, New York, 2004.
[15] L. Evans, Partial Differential Equations, Graduate Studies in Mathematics, vol. 19, American Mathematical Society, 2009.
[16] G.N. Gatica, A. Márquez, M.A. Sánchez, Analysis of a velocity–pressure–pseudostress formulation for the stationary Stokes equations, Comput. Methods Appl. Mech. Eng. 199 (2010) 1064.

[17] G. Hashimoto, K. Ono, A fixed Eulerian mesh-based scheme using level set function for airbag deployment simulation including the effect of outside air, in: J. Pereira, A. Sequeira (Eds.), V European Conference on Computational Fluid Dynamics, 2010.
[18] A. Hirth, A. Haufe, L. Olovsson, Airbag simulation with LS-Dyna: past–present–future, in: 6th European LS-Dyna Users' Conference, 2007.
[19] G. Hsiao, W. Wendland, Boundary element methods: foundation and error analysis, Fundamentals of Encyclopedia of Computational Mechanics, vol. 1, John Wiley & Sons, Ltd., Chicester, 2004, pp. 339–373 (Chapter 12).
[20] T. Hughes, W. Liu, T. Zimmermann, Lagrangian–Eulerian finite element formulation for incompressible viscous flows, Comput. Methods Appl. Mech. Eng. 29 (1981) 329–349.
[21] U. Küttler, C. Förster, W.A. Wall, A solution for the incompressibility dilemma in partitioned fluid–structure interaction with pure Dirichlet fluid domains, Comput. Mech. 38 (2006) 417–429.
[22] S. Liapis, An adaptive boundary element method for the solution of potential flow problems, Eng. Anal. Boundary Elem. 18 (1996) 29–37.
[23] J. Lions, E. Magenes, Non-Homogeneous Boundary Value Problems and Applications I, Springer-Verlag, Berlin, 1972.
[24] P.-O. Marklund, L. Nilsson, Simulation of airbag inflation processes using a coupled fluid structure approach, Comput. Mech. 29 (2002) 289–297.
[25] U. Mayer, A. Popp, A. Gerstenberger, W. Wall, 3d fluid–structure-contact interaction based on a combined 3D fluid–structure-contact interaction based on a combined XFEM FSI and dual mortar contact approach, Comput. Mech. 46 (2010) 53–67.
[26] W. McLean, Strongly Elliptic Systems and Boundary Integral Equations, Cambridge University Press, 2000.
[27] J. Monaghan, Smoothed particle hydrodynamics, Annual Review of Astronomy and Astrophysics, vol. 30, Annual Reviews Inc., 1992, pp. 543–574.
[28] J. Rungamornrat, M. Mear, SGBEM–FEM coupling for analysis of cracks in 3d anisotropic media, Int. J. Numer. Methods Eng. (2011) 224–248.
[29] P. Saksono, W. Dettmer, D. Perić, An adaptive remeshing strategy for flows with moving boundaries and fluid–structure interaction, Int. J. Numer. Methods Eng. 71 (2007) 1009–1050.
[30] S. Sauter, C. Schwab, Boundary Element Methods, Springer, 2010.
[31] E. Stephan, Coupling of boundary element methods and finite element methods, Fundamentals of Encyclopedia of Computational Mechanics, vol. 1, John Wiley & Sons, Ltd., Chicester, 2004, pp. 375–412 (Chapter 13).
[32] E.P. Stephan, M. Maischak, A posteriori error estimates for FEM–BEM couplings of three-dimensional electromagnetic problems, Comput. Methods Appl. Mech. Eng. 194 (2005) 441–452. Selected papers from the 11th Conference on The Mathematics of Finite Elements and Applications.
[33] K. Takizawa, T. Spielman, T. Tezduyar, Space–time FSI modeling and dynamical analysis of spacecraft parachutes and parachute clusters, Comput. Mech. 48 (2011) 345–364.
[34] T. Tezduyar, Stabilized finite element formulations for incompressible flow computations, Adv. Appl. Mech. 38 (1992) 1–44.
[35] T. van Opstal, P. Bauman, S. Prudhomme, E. van Brummelen, Goal-oriented model adaptivity for viscous incompressible flows, Tech. Report 13-07, Institute for Computational Engineering and Science, The University of Texas at Austin, 2013.
[36] T. van Opstal, E. van Brummelen, A potential-flow BEM for large-displacement FSI, CASA-Report 12-03, University of Technology, Eindhoven, 2012.
[37] T. van Opstal, E. van Brummelen, R. de Borst, M. Lewis, A finite-element/boundary-element method for large-displacement fluid–structure interaction, Comput. Mech. 50 (2012) 779–788.
[38] S.K. Veerapaneni, A. Rahimiany, G. Biros, D. Zorin, A fast algorithm for simulating vesicle flows in three dimensions, J. Comput. Phys. 230 (2010) 5610–5634.
[39] T. Wick, Fully Eulerian fluid–structure interaction for time-dependent problems, Comput. Methods Appl. Mech. Eng. 255 (2013) 14–26.
[40] L. Wrobel, The Boundary Element Method, Applications in Thermo-Fluids and Acoustics, vol. 1, John Wiley & Sons, 2002.
[41] D. Yong, Strings, chains and ropes, SIAM 48 (2006) 771–781.
[42] A. York, D. Sulsky, H. Schreyer, Fluid-membrane interaction based on the material point method, Int. J. Numer. Methods Eng. 48 (2000) 901–924.
[43] O. Zienkiewicz, D. Kelly, P. Bettess, The coupling of the finite element method and boundary solution procedures, Int. J. Numer. Methods Eng. 11 (1977) 355–375.